

# Politecnico di Torino

Master's Degree in Biomedical Engineering

# CT-based Finite Element Modeling of the human femur: comparison with in-vitro strain measurements under stance loading conditions

Candidate: Sara Santucci

Supervisor: Dott.ssa Alessandra Aldieri

Co-Supervisor: Prof.ssa Cristina Bignardi

#### Abstract

Proximal femoral fractures are among the most common osteoporosis-related injuries and are projected to affect roughly 21 million individuals worldwide by 2025. These fractures occur predominantly as a consequence of falls, but may also arise as spontaneous failures under paraphysiological loading, particularly in older adults with osteoporosis, who exhibit reduced bone mineral density (BMD). Although BMD is clinically employed to estimate fracture risk, this latter ultimately depends on bone strength—the capacity of bone to withstand physiological, paraphysiological, and pathological loads—which is not fully captured by BMD alone. Computed Tomography (CT)-based finite element (FE) modeling could represent a valid alternative to estimate in vivo the subject-specific femur strength. Yet, such models need to be first validated against experimental in vitro data. The aim of this thesis was thus to construct CT-based FE models of four human cadaveric femurs, reproducing the in-vitro experimental tests previously conducted on the same specimens to compare the models' predictions with the experimental outcomes. In the experimental set up all femurs were instrumented with up to 16 triaxial strain gauges and subjected to six loading configurations that span the entire cone of the hip joint resultant force while standing, including the single leg stance configuration and the most relevant loading configuration for spontaneous fractures (8° in the frontal plane). Corresponding boundary conditions were applied to the FE models built starting from the specimens CT images and simulated using Ansys Mechanical APDL. Principal strains were extracted at nodes in the same location as the strain gauges and averaged over a sphere of 3mm to ensure continuity of the strain and avoid local effects. The principal strains values predicted by the models could then be compared with the experimental measurements obtained for each strain gauge on each femur and for all loading configurations. To assess the accuracy of the models, regression analyses of predicted vs experimental strains were carried out separately for each femur, for paired and unpaired femurs, and for the entire set of specimens pooled across the six loading configurations, taking into account both maximum and minimum principal strains. Model errors were quantified using the RMSE and the maximum peak error, expressed both in microstrain and as a percentage of the maximum absolute experimental strain. All models showed remarkable predictive accuracy, as results for all femurs pooled together yielded a high determination coefficient ( $R^2$ =0.89) and slope and intercept of the regression line almost one and zero respectively; moreover, the RMSE is 118 με (12% of the highest measured strain in absolute values), which is minimally worse than the experimental findings, in which a RMSE of 113 με (10% of the highest measured strain) is reported. It is sensible to assume that this slight discrepancy might be due to uncertainties related to the segmentation process or to strain gauges measurements. Nonetheless, the strain distribution reported by the models across all femurs

and all six loading configurations exhibits the expected biomechanical pattern. Tensile strains ( $\epsilon_1$ ) dominated on the lateral aspect of the proximal femur, with peak values ranging from 707  $\mu\epsilon$  to 927  $\mu\epsilon$ , and compressive strains ( $\epsilon_3$ , in absolute values) were predominant on the medial aspect, with peak values ranging from  $-746~\mu\epsilon$  to  $-835~\mu\epsilon$ , consistent with experimental observations.

In conclusion, the subject specific CT-based FE models developed in this thesis successfully reproduced the experimental protocol and accurately predicted both maximum and minimum principal strains. Furthermore, such models were able to replicate the experimental strain distribution under stance loading conditions with notable results, showing the expected pattern of higher tensile strains and higher compressive strains on the lateral and medial aspect of the femur, respectively. Future developments may include a refinement of the segmentation process, as it might enhance the predictive accuracy of the models. Furthermore, these models might also be applied to a larger pool or femurs, or adapted to simulate different loading scenarios, such as sideways falls.

# TABLE OF CONTENTS

LIST OF FIGURES	
LIST OF TABLES	
1 INTRODUCTION	
1.2 Bones Classification	
1.3 Bone Tissue and Biomechanics	9
1.4 Osteoporosis	11
1.5 Proximal Femur Fractures	11
1.6 Finite element analysis	12
1.7 CT-based patient specific finite element models	12
1.8 Aim of the thesis	15
2 MATERIALS AND METHODS	
2.2 Experimental procedure	
2.2.1 Marking of the anatomical reference system	
2.2.2 Strain Gauges Placement	
2.2.3 Loading scenario	
2.3 Subject-Specific CT-based FE model	
2.3.1 Segmentation	
2.3.2 CT Reference System	23
2.3.3 Definition of the anatomical reference system	26
2.3.4 Identification the strain gauges positions on MATLAB	
2.3.5 Meshing	42
2.3.6 Assignment of non homogeneous material properties	43
2.3.7 Finite Element Analysis	
2.3.8 Comparison between predicted and experimental values	52
3 RESULTS	53
3.1 Results per femur	53
3.2 Paired and un-paired interspecimen results	57
3.3 Results by pooling all femurs	61
4 DISCUSSION	
5 CONCLUSION	
IN DATE TAIN TAIN TO TAIN. TAND	

# LIST OF FIGURES

Figure 1.1-1. Anatomy of the femur7
Figure 1.2-1 Different sections of a long bone. A femur is represented, highlighting the three anatomical regions of a long, diaphysis, metaphysis and epiphysis
Figure 1.2-2. Internal structure of cortical and trabecular bone. The main structural unit of cortical bone is the osteon, consisting of concentric lamellae arranged around a central Haversian canal, which contains blood vessels and nerve fibers9
Figure 2.2-1. Left femur with the anterior side up, the location of the two landmarks is shown.  Credits to [33]17
Figure 2.2-2. Femur in the clamping ring to mark the sagittal plane. Both condyles must contact the plate. Credits to [33]
Figure 2.2-3. Left femur placed on a level surface supported by the clamping ring to mark the sagittal plane. Credits to [33]
Figure 2.2-4. Proximal metaphysis of a left femur, anterior and lateral views. The position of the strain gauges based on fractions of BL and HD is shown. Credits to [35]. © Elsevier. Reproduced with permission
Figure 2.2-5. Anterior and lateral views of a right femur. The direction of the hip joint force for the six different loading configurations is shown, both in the frontal and in the sagittal plane. LC1-LC4 cover the extreme angle of the hip resultant force in the normal, and sagittal plane; LC5 is applied parallel to the femoral diaphysis; LC6 is tilted of 8° in the frontal plane to replicate the most relevant condition for spontaneous fractures. Credits to [17], © Elsevier. Reproduced with permission.
Figure 2.3-1. Segmentation of femurs #3154 (a) and #3155 (b) imported into Paraview to highlight the partial reconstruction of the missing slice, which appears as a slight necking in the metaphyseal region.
Figure 2.3-2. Experimental strain gauges placed on femur #3154 (Donor#2 right femur) after importing the point cloud in the STL file in MATLAB. a) anterior view; b) posterior view. The coordinates of the experimental strain gauges reported in Table 2.3-1 are referred to the CT reference system
Figure 2.3-3. Experimental strain gauges placed on femur #2921 (Donor#1 left femur) after importing the point cloud in the STL file in MATLAB. a) anterior view; b) posterior view. The coordinates of the experimental strain gauges reported in Table 2.3-2 are referred to the CT reference system
Figure 2.3-4. Femur #3154 (Donor#2 right femur) resting anterior side up on a plane defined by the lesser trochanter and the two condyles. a) lateral view, b) medial view26
Figure 2.3-5. Femur #3154 (Donor#2 right femur), preparing for marking of the sagittal plane. The two landmarks on the anterior side are found as midthicknesses at the level of the flat regions just below the lesser trochanter and above the intercondylar fossa respectively. a) anterior side view, b) medial side view.

Figure 2.3-6. Femur #3154 (Donor#2 Right femur), marking of the sagittal plane. a) The two landmarks on the anterior side are made horizontal by rotating the femur; b) The two landmarks are then aligned vertically as well.
Figure 2.3-7. Femur #3154 (Donor#2 right femur), preparing for marking of the frontal plane. The two landmarks on the medial side are found as midthicknesses of the anterior-posterior widths at the same two levels as before.
Figure 2.3-8. Femur #3154 (Donor#2 right femur), marking of the frontal plane. The two landmarks on the medial side made horizontal.
Figure 2.3-9. Proximal metaphysis of a left femur, anterior and lateral views. The position of the strain gauges A0, P0 on the metaphysis and of strain gauges A1, L1, M1 on the metaphysis is depicted. Credits to [35]. © Elsevier. Reproduced with permission30
Figure 2.3-10. Femur #3154. Visualization of experimental strain gauge placement (in red) and computationally determined strain gauge locations (in black) for the metaphysis of the femur. Views are presented from the (a) anterior and (b) posterior sides, corresponding respectively to the positions of strain gauges A0 and P0, in order to highlight both experimental and computed placements
Figure 2.3-11 Femur #3154. Visualization of experimental strain gauge placement (in red) and computationally determined strain gauge locations (in black) for the diaphysis region of the femur. Views are presented from the (a) anterior, (b) lateral, and (c) medial sides, corresponding respectively to the positions of strain gauges A1, L1, and M1, in order to highlight both experimental and computed placements.
Figure 2.3-12. Femur #3154, frontal (a) and sagittal (b) plane. Isolation of the neck region (in cyan) and computation of the anatomical neck axis (in red)
Figure 2.3-13. Femur #3154. The femur was rotated so that the neck axis (in red) could become parallel to the vertical axis of the diaphysis. The two landmarks defining the frontal plane (a) and the two landmarks defining the sagittal plane (b) are also shown
Figure 2.3-14. Femur #3154, visualized in the XZ plane (a) and YZ plane (b). The femur was rotated by 45° in the frontal plane, allowing the actual neck axis to be considered as aligned with the vertical axis, i.e., perpendicular to the ground
Figure 2.3-15. Femur #3154. Visualization of experimental strain gauge placement (in red) and computationally determined strain gauge locations (in black) for the head region of the femur. Views are presented from the (a) anterior, (b) lateral, (c) medial, and (d) posterior sides, corresponding respectively to the positions of strain gauges AH, LH, MH, and PH, in order to highlight both experimental and computed placements.
Figure 2.3-16. Femur #3154. Visualization of experimental strain gauge placement (in red) and computationally determined strain gauge locations (in black) for the neck region of the femur. Views are presented from the (a) anterior, (b) lateral, (c) medial, and (d) posterior sides, corresponding respectively to the positions of strain gauges AN, LN, MN, and PN, in order to highlight both experimental and computed placements.
Figure 2.3-17. Femur #2921. Visualization of experimental strain gauge placement (in red) and computationally determined strain gauge locations (in black) for the metaphysis of the femur. Views are presented from the (a) anterior, (b) lateral, (c) medial, and (d) posterior sides, corresponding

respectively to the positions of strain gauges A0, L0, M0, and P0, in order to highlight both experimental and computed placements38
Figure 2.3-18. Femur #2921. Visualization of experimental strain gauge placement (in red) and computationally determined strain gauge locations (in black) for the proximal diaphysis of the femur. Views are presented from the (a) anterior, (b) lateral, and (c) medial sides, corresponding respectively to the positions of strain gauges A1, L1, and M1, in order to highlight both experimental and computed placements.
Figure 2.3-19. Femur #2921. Visualization of experimental strain gauge placement (in red) and computationally determined strain gauge locations (in black) for the head region of the femur. Views are presented from the (a) anterior, (b) lateral, (c) medial, and (d) posterior sides, corresponding respectively to the positions of strain gauges AH, LH, MH, and PH, in order to highlight both experimental and computed placements
Figure 2.3-20. Femur #2921. Visualization of experimental strain gauge placement (in red) and computationally determined strain gauge locations (in black) for the neck region of the femur. Views are presented from the (a) anterior, (b) medial, and (c) posterior sides, corresponding respectively to the positions of strain gauges AN, MN, and PN, in order to highlight both experimental and computed placements.
Figure 2.3-21. Before the actual meshing process in Hypermesh 2019, femur #3154 has been isotropically remeshed in MeshLab to enhance the quality of the STL obtained from 3DSlicer and prevent further complications during the realization of the 3D mesh. The resulting femoral surface is a single, continuous component composed of triangular elements
Figure 2.3-22. 10-node tetrahedral 3D mesh of femur #3154 obtained in Hypermesh 2019. The central portion of the femur has been masked to illustrate that the mesh is fully solid
Figure 2.3-23. Segmentation of the phantom used to calibrate the CT dataset for all femurs. Three separate segmentations were performed for the inserts representing the spinal process, cancellous bone, and cortical bone, shown in yellow, green, and red, respectively. Using the Segment Statistics tool, the mean HU value for each insert was obtained (highlighted in the red box in the figure), showing an increase in HU corresponding to increasing insert density
Figure 2.3-24 Regression line for femurs #2920, #2921, #3154, #3155
Figure 2.3-25. The 3D mesh for femur #3154 has been imported into Bonemat Rolling and visualized
Figure 2.3-26. Femur #3154. ANSYS .CDB file generated with Bonemat Rolling for femur #3154, imported into Paraview to visualize the spatial distribution of the material properties assigned to each finite element
Figure 2.3-27. The six loading configurations, shown as a single force directed onto the head of the femur at different inclinations, are here represented on a right femur. Credits to [17]. © Elsevier. Reproduced with permission
Figure 2.3-28. The constraints from $zth = zmax$ , $head - 0.33 * BL - 100mm$ up to the point with the lowest z-coordinate are applied on LC5 (neutral configuration) for femur #3154. The femur is rotated by $0^{\circ}$ in the frontal plane and $0^{\circ}$ in the sagittal plane. Constrains are defined within a local reference system that accounts for this rotation
Figure 2.3-29. The force is applied on LC5 (neutral configuration) for femur #3154. The femur is rotated by 0° in the frontal plane and 0° in the sagittal plane. The load is applied along the global z-

axis in order to replicate the experimental procedure. Both the XZ-plane (a) and YZ-plane (b) visualizations are shown
Figure 2.3-30. ROI for LC5 (neutral configuration) of femur #3154. The 10-node tetrahedral elements forming the mesh are second-order elements, meaning that additional nodes are located at the midpoints of each edge of the tetrahedron. These mid-edge nodes are not considered when selecting the ROI.
Figure 2.3-31. The constraints from $zth = zmax$ , $head - 0.33 * BL - 100mm$ up to the point with the lowest z-coordinate are applied femur #3154. Constrains are defined within a local reference system that accounts for this rotation. The six loading configurations are shown. Load application is carried out within the global reference system.
Figure 3.1-1. Scatter plots for the regression analyses, computed using only the strain gauges common to all femora. Data points for the femora with experimentally measured gauge locations—#3154 (Right 2) and #2921 (Left 1)—are shown in blue; data points for the remaining femora—#2920 (Right 1) and #3155 (Left 2)—are shown in purple
Figure 3.2-1. Linear regression of predicted strains vs experimental strains for paired femurs #2920-#2921 (Donor #1) and paired femurs #3154-#3155 (Donor #2). All strain measurements are plotted (\varepsilon_1 and \varepsilon_3) for all strain gauges present on both femurs in each pair. Femurs whose strain gauges experimentals positions were available (#2921- Left 1 and #3154-Right 2) are scattered in blue; data points for the remaining femora—#2920 (Right 1) and #3155 (Left 2)—are shown in purple.
Figure 3.2-2. Regression lines obtained for two cross-pairs of femurs, highlighting the difference in predictive accuracy between specimens for which the experimental strain gauge positions were available (femurs #2921, Left 1, and #3154, Right 2; shown in blue) and those for which they were not (femurs #2920, Right 1, and #3155, Left 2; shown in purple)
Figure 3.3-1. Linear regression of predicted strains vs experimental strains for all pooled femurs. All strain measurements are plotted ( $\varepsilon_1$ and $\varepsilon_3$ ) for all strain gauges. Data points corresponding to femurs with experimentally verified strain gauge locations are shown in blue, while those from the other two femurs are represented in purple.

# LIST OF TABLES

Table 2.2-1. Directions of the six loading configuration with respect to the vertical axis in the frontal $(\alpha)$ and sagittal $(\beta)$ plane	22
Table 2.3-1. Experimental coordinates (in mm) of the strain gauges of femur #3154 (Donor #2) referred to the CT reference system	23
Table 2.3-2. Experimental coordinates in mm of the strain gauges of femur #2921 (Donor #1) referred to the CT reference system	24
Table 2.3-3. Distances between experimental strain gauges computationally determined strain gauges in the metaphyseal region. Distances were calculated between the strain gauges placed level 0 and the experimental strain gauges labeled A1 and P1, reflecting the change in nomenclature as previously described	at 31
Table 2.3-4. Distances between experimental strain gauges computationally determined strain gauges in the metaphysis region. Distances were calculated between the strain gauges placed a level 1 and the experimental strain gauges labeled A3, L3, and P3, reflecting the change in nomenclature as previously described.	nt 32
Table 2.3-5. Distances between experimental strain gauges and computationally determined str	rain 35
Table 2.3-6. Distances between experimental strain gauges and computationally determined str	rain 37
Table 2.3-7. Distances between experimental strain gauges and computationally determined str gauges in the metaphyseal region. Distances were calculated between the strain gauges placed level 0 and the experimental strain gauges labeled A1, L1, M1 and P1, reflecting the change in nomenclature as previously described	at
Table 2.3-8. Distances between experimental strain gauges and computationally determined str gauges in the diaphysis region. Distances were calculated between the strain gauges placed at 1 and the experimental strain gauges labeled A3, L3, and P3, reflecting the change in nomenclass previously described	level
Table 2.3-9. Distances between experimental strain gauges and computationally determined str	
Table 2.3-10. Distances between experimental strain gauges and computationally determined strain gauges in the neck region	
Table 2.3-11. Directions of the six loading configuration with respect to the vertical axis in the frontal $(\alpha)$ and sagittal $(\beta)$ plane	47
Table 3.1-1. Validation Parameters for femur #2920 (Right 1)	55
Table 3.1-2. Validation Parameters for femur #2921 (Left 1)	55
Table 3.1-3. Validation Parameters for femur #3154 (Right 2)	55
Table 3.1-4. Validation Parameters for femur #3155 (Left 2)	56
Table 3.2-1. Validation Parameters for Donor #1	58
Table 3.2-2. Validation Parameters for Donor #2	58

Table 3.2-3. Validation Parameters for unpaired femurs #2921 (Left 1) and #3154 (Right 2), v	vhich
were the only two femurs whose experimental strain gauges positions were available	60
Table 3.2-4. Validation Parameters for unpaired femurs #2920 (Right 1) and #3155 (Left 2), vexperimental strain gauges positions were not available	
Table 3.3-1. Validation Parameters for all pooled femurs	62

# 1 INTRODUCTION

# 1.1 Anatomy of the femur

The femur is classified as a long bone and is located in the thigh region. It is the largest bone by volume in the human skeleton and bears a substantial proportion of body weight. Proximally, it articulates with the acetabulum of the hip; distally, it articulates with the tibia and the patella, thereby forming the knee joint [1].

The proximal femur consists of the head, neck, and the greater and lesser trochanters. The femoral head, approximately spherical, articulates with the acetabulum to constitute the coxofemoral (hip) joint, which, together with the knee, enables locomotor activities such as walking, running, and stair climbing. The head continues into the anatomical neck, at the base of which lie the greater trochanter (quadrangular in shape and situated superiorly), and the lesser trochanter, a conical eminence directed postero-medially. These prominences represent principal sites of muscular attachment [2].

The distal femur, broader than the remainder of the bone, serves as the primary interface for load transmission to the tibia. It comprises the medial and lateral condyles, ovoid masses with a predominant anteroposterior axis. Posteriorly, the condyles are separated by the intercondylar fossa; anteriorly, they articulate with the patella via the femoral trochlea. Superior to the condyles lie the medial and lateral epicondyles, which constitute important attachment sites for ligaments and muscles [3].

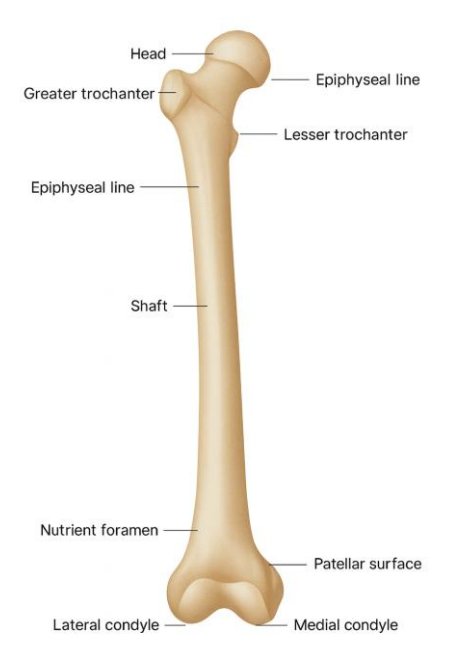


Figure 1.1-1. Anatomy of the femur

#### 1.2 Bones Classification

Bones can be classified according to anatomic features and structural composition [4].

Anatomically, they can be divided into flat, irregular, sesamoid, short, and long bones based on their shape [5]. Long bones, such as the femur, present three anatomical zones [6], as also shown in Figure 1.2-1:

- Diaphysis, namely the shaft
- Epiphysis, at the two ends of the shaft and usually responsible for articulation
- Metaphysis, between diaphysis and metaphysis

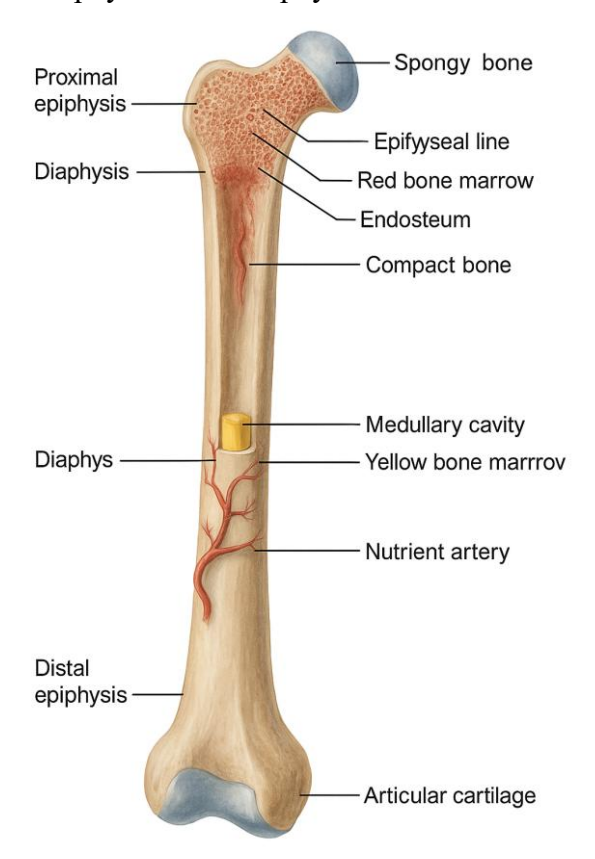


Figure 1.2-1 Different sections of a long bone. A femur is represented, highlighting the three anatomical regions of a long, diaphysis, metaphysis and epiphysis.

On the other hand, when looking at the macroscopic structure of bone tissue, a distinction can be made between cortical and trabecular bone. Cortical bone makes up the dense outer layer of bones and represents 80% of the total bone tissue, while trabecular bone is a porous and spongy structure that can be found in the inner region of short and flat bones and at the epiphyses of the long bones [6].

Cortical bone is composed of repeating structural units known as osteons, each consisting of concentric lamellae of bone tissue arranged around a central channel, the Haversian canal, which contains blood vessels and nerve fibers. Trabecular, or cancellous, bone consists of a three-

dimensional network of trabeculae, which are composed of parallel layers of lamellar bone. The intertrabecular spaces are occupied by bone marrow [5].

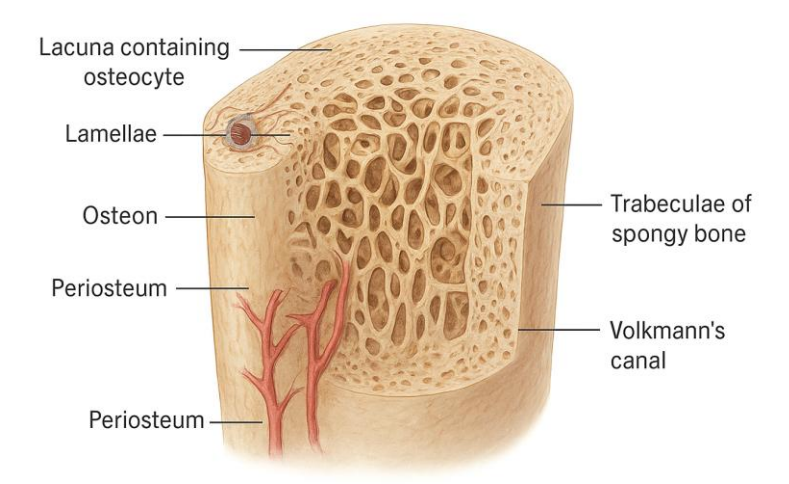


Figure 1.2-2. Internal structure of cortical and trabecular bone. The main structural unit of cortical bone is the osteon, consisting of concentric lamellae arranged around a central Haversian canal, which contains blood vessels and nerve fibers.

Diaphysis of long bones mainly consists of cortical bone that hosts the medullar cavity where the bone marrow is held, while the metaphysis and the epiphyses present a larger quantity of trabecular bone surrounded by a thin cortical layer [7].

#### 1.3 Bone Tissue and Biomechanics

Bone is a connective tissue whose extracellular matrix is mineralized [6] and that shows four types of cells: osteoblasts, osteocytes, osteoclasts, and bone lining cells [8].

Bones serve as reservoirs of vital minerals, contain sites for blood cell formation and provide structural support, mobility, and protection to the body. Bones are not static structures and bone remodeling continuously occurs in response to external stimuli and physiological needs [8].

Bone formation is mainly driven by osteoblasts, that are responsible for the production of osteoid, which is then mineralized into the extracellular matrix. The latter is indeed composed of 40% organic material (mainly collagen and proteoglycans) and 60% inorganic material (hydroxyapatite Ca10(PO4)6(OH)2)[9], making it the body's main store of calcium and phosphate [8]. The presence of both mineral and organic content allows for both resilience and strength, for a structure made of collagen and proteoglycans only would be excessively flexible, whereas a totally mineral one would be very hard and brittle [4].

During mineralization osteoblasts become osteocytes incorporated into the bone matrix. Osteocytes have a mechanosensitive function and convert mechanical stimuli into biochemical signals. Bone resorption is due to osteoclasts, multinucleated cells that secret acid (to degrade hydroxyapatite) and collagenase (to degrade the organic components). Proper skeletal function and calcium homeostasis require a tightly coupled balance between osteoclastic resorption and osteoblastic formation [8].

The remodeling cycle proceeds through successive phases: a quiescent phase during which lining cells protect the surface; activation/resorption, in which precursors differentiate into osteoclasts that remove mineralized bone; a reversal phase, during which reversal cells prepare the surface; and formation, in which osteoblasts deposit osteoid that subsequently mineralizes. A complete cycle typically lasts 3–6 months [10]. Although the precise role of bone-lining cells is not fully defined, current evidence suggests their participation in the coordinated regulation of resorption and formation. Dysregulation of this coupling leads to skeletal disfunctions, and excess resorption in particular reduces bone mass and predisposes to osteoporosis [8].

From a structural prospective, cortical bone is significantly denser than trabecular bone, thereby contributing predominantly to the mechanical strength of the skeleton [5]. In contrast, trabecular bone is more porous, offering an extensive surface area that facilitates mineral exchange [5]. Although its stiffness is considerably lower than that of cortical bone, the orientation of its trabeculae along principal load paths enables efficient load transfer to the surrounding cortical bone, optimizing the overall mechanical performance of the structure [11].

While the trabecular–cortical architecture yields a structure that is both lightweight and strong, bone should not be regarded as a homogeneous two-phase composite; recent studies characterize it as inhomogeneous, anisotropic [12], and with a viscoelastic behavior [13].

This means that the mechanical characteristics of bones vary according to the magnitude, rate of application and direction of the applied load; in particular, the strength and rigidity of a bone are higher in the direction of the daily loads it's subjected to. Furthermore, mechanical properties may also depend on the composition of bone, which changes based on the anatomical position, and on the aging of the bones themselves [13]. Therefore, the connection among composition, geometry and mechanical properties shows the relevance of the relationship between form and function in bone biomechanics [11].

Biomechanics of bones can be thus assed at two different levels, namely the tissue level (by implementing standard mechanical tests on samples of uniform bone tissue) and the structural level

(by analyzing the behavior of the whole bone as a unit). These presence of these two levels is also shown when fractures occur, since the failure concerns both the bone structure and tissue [13].

### 1.4 Osteoporosis

Osteoporosis is a multifactorial skeletal disorder characterized by a reduction in bone mass and deterioration of trabecular and cortical microarchitecture, thereby increasing susceptibility to fracture—most notably of the femur—even following low-energy trauma. Peak bone mass is achieved during adolescence and is maintained in adulthood until perturbations of the remodeling process occur; such derangements disrupt the coupling between osteoblast-mediated formation and osteoclast-mediated resorption. The condition is more prevalent in women, in whom the progressive decline in estrogen production, culminating in menopause, represents the predominant sex-specific risk. Preventive strategies include adequate intake of calcium and vitamin D, together with the maintenance of muscle strength. Risk determinants encompass both intrinsic, non-modifiable factors (age, sex, ethnicity) and modifiable factors (diet, lifestyle, and medical comorbidities) [14].

#### 1.5 Proximal Femur Fractures

Proximal femur fractures are one of the most common types of fracture and it's estimated that their incidence will increase to 21 million people annually by 2050. Risk factors for hip fractures are numerous and range from neurological diseases to gait anomalies, to osteoporosis, and they are based on two main factors [15]:

- The proximal femur strength, namely the maximum physiological, paraphysiological, or pathological load applied to the femoral head that the proximal femur can withstand [16].
- The risk of an event leading to a force on the femoral head greater than the proximal femur strength occurring.

Fractures that affect proximal femur are mostly due to falls [17], but also spontaneous fractures (namely those fractures that care not caused by traumatic events but by para-physiological and sudden excessive loadings) occur, especially in osteoporotic elderly subjects [18]. These ones are indeed affected by a progressive decrease in bone density due to an excessive osteoclastic activity, that results in weakened and more brittle bones that may fracture more easily [19].

At present, the clinical standard for diagnosing osteoporosis and estimating proximal femur fracture risk is areal bone mineral density (aBMD). BMD is measured by dual-energy X-ray absorptiometry (DXA) and combined with clinical risk factors in tools, such as FRAX, to compute the 10-year probability of osteoporotic fracture based on age, sex, body habitus, comorbidities, and lifestyle. DXA employs two X-ray beams at different energies to subtract soft-tissue attenuation. It offers high

precision at low radiation dose, but yields only two-dimensional measurements that do not take into account the geometry of the bone [20].

More recently, computer tomography (CT) has been progressively used more to diagnose osteoporosis and assess fracture risk [20]. CT requires rotating X-ray projections to reconstruct tomographic slices that can be stacked into a three-dimensional image [21]. Compared with DXA, CT involves a higher radiation dose, but provides several advantages: true 3-D information and separate quantification of trabecular and cortical compartments [20]. This distinction is clinically relevant because trabecular bone is more metabolically active and may then offer earlier evidence of response to a particular therapy, whereas cortical bone contributes more to overall bone strength and fracture resistance [22].

Risk assessment and fracture prediction can be further improved by implementing CT-based finite elements (FE) models, as such models incorporate both individual bone geometry and subject-specific tissue-level mechanical properties [23].

# 1.6 Finite element analysis

Finite element analysis (FEA) is a robust numerical approach that has become widely adopted across various engineering disciplines, including biomechanics. It is founded on the finite element method (FEM) and consists of discretizing the geometric domain into smaller, interconnected subdomains, commonly referred to as elements, that present simple geometrical shapes such as triangles and tetrahedra. Each vertex within these elements is designated as a node, and the collective arrangement of these nodes forms a computational grid known as a mesh. The mesh encapsulates critical information regarding the mechanical properties and behavior of the structure under analysis [24]. Finite element (FE) models allow therefore the computation of determined physical quantities, such as stress and strain, over the entire domain instead of fewer selected points [16].

# 1.7 CT-based patient specific finite element models

CT-based patient specific FE models are currently the only available method to non-invasively estimate mechanical stresses [12] and to non-destructively evaluate bone strength in vivo [25], with the ultimate goal of being employed in clinical settings to predict osteoporotic fracture risk at a stage when preventive or therapeutic interventions are still feasible [26]. Their translation into routine clinical practice, however, is still limited, mainly because they require a high level of automation as well as careful accuracy assessment through experimental validation [26]. This last point is crucial when talking about assessment of risk fracture in the proximal femur, because this area is characterized by spongious bone surrounded by a very thin shell of cortical bone, and thus by a remarkable local non-homogeneity [12].

CT based subject specific FE models are built through a sequence of operations that begin with the segmentation of CT datasets to extract the 3D surfaces of the bone, which are successively converted into NURSB models with reverse-engineering software Geomagic Studio (v. 6, Raindrop Geomagic, Inc., USA). From this surface, a 10-noded tetrahedral finite element mesh is automatically generated by using Hypermesh (Altair Engineering, Inc., USA). Onto this mesh, non-homogeneous mechanical properties are assigned. Initially, this part of the procedure consisted of giving an average Hounsfield Unit (HU) number to each element of the mesh by numerically integrating the HU field over the element's volume using the in-house developed software Bonemat\_V2. A calibration phantom (European Spine Phantom) was then used to calibrate the CT dataset. Finally, by assuming a linear relationship between HU average values and ash density, it was possible to assign a different Young's Modulus (E) to each element of the mesh based on the density information contained in the CT dataset [12].

The resulting model was evaluated through a sensitivity analysis based on a Monte Carlo simulation, in which geometry, material properties, and density were treated as random input variables, while the most commonly used biomechanical indicators served as output variables. Although the influence of geometry, material properties, and density on the outputs cannot be determined *a priori*, the approach demonstrated sufficient accuracy to be reliably employed [23]. More recently, particular attention has been devoted to further improving the assignment of material properties, refining the material-mapping strategy and clarifying the relationship between bone density and mechanical properties in order to achieve more robust and accurate results [26].

Concerning the material mapping strategy, it has been demonstrated that, rather than averaging the Hounsfield Unit (HU) values over each finite element and subsequently deriving the corresponding Young's modulus (E), more accurate results are achieved by first converting each HU voxel value directly into its corresponding E voxel value. The resulting scalar field of E values is then averaged over each element. This improved approach has been implemented using an enhanced version of the software Bonemat, BonematV3 [27].

Regarding the relationship between E and density, the calibration of the CT dataset is a crucial step. A calibration phantom is a body characterized by insertions of calcium hydroxyapatite or potassium diphosphate [28] at different concentrations in order to represent the spinal process, cortical and trabecular bone with known density values  $\rho_{QCT}$ [29]. The European Spine Phantom (ESP) contains three certified hydroxyapatite solution inserts of 50, 100 and 200 mg/cm3, respectively [28].

The relationship between Young's modulus (E) and density ( $\rho$ ) plays a critical role in determining the accuracy of strain predictions in finite element models [26]. In order to assess the influence of such

relationships on the model's outcomes, a study that will be used as reference study in this thesis compared three different empirical relationships between density and modulus:

(1) 
$$E = 3.790 \rho_{app}^3$$
 (Carter and Hayes; 1977)

(2) 
$$E = 10.500 \rho_{ash}^{2.29}$$
 (Keller; 1994; femoral specimens)

(3) 
$$E = 6.950 \rho_{app}^{1.49}$$
 (Morgan et al.; 2003; femoral neck specimens)

E denotes the modulus of elasticity in gigapascals (GPa),  $\rho_{app}$  the apparent density and  $\rho_{ash}$  the ash density, both in grams per cubic centimeter (g/cm<sup>3</sup>) [26].

Apparent density  $\rho_{app}$  is the density in fresh and wet conditions. After measuring the bulk volume of bone specimens, these were washed to remove the bone marrow and then air jetted and weighed until two consecutive weight measurements presented a mass difference under 0.5%;  $\rho_{app}$  was then computed as wet weight/bulk volume [28]. Analogously,  $\rho_{ash}$  was calculated as ash weight/bulk volume after burning the specimen for 24 hours at 650° and an additional 24 hours of cooling [28].

The highest predictive accuracy was achieved using the relationship proposed by (Morgan et al., 2003), that has been established with an extrapolation over the full range of apparent densities considered [26]. Nonetheless, it has been pointed out [28] that, since this relationship requires apparent density, some assumptions are still needed; indeed, the CT data can only offer information about the bone radiological density  $\rho_{OCT}$ , related to bone mineral content. Two main hypotheses were therefore that  $\rho_{OCT}$  was equal to  $\rho_{ash}$  and the ratio  $\rho_{ash}/\rho_{app}$  was equal to a value found in literature. The former assumption has been then refuted because phantoms and bone present differences in their mineral composition and thus phantoms cannot perfectly replicate bone attenuation coefficient; furthermore, phantoms mineral insertions, be either calcium hydroxyapatite or potassium diphosphate, are homogenous, while bone insertions, trabecular bone at CT dataset resolution in particular, are non-homogenous. Owing to the strong correlation between  $ho_{QCT}$  and  $ho_{ash}$  , a linear correction of the phantom-calibrated  $\rho_{QCT}$  density was implemented to effectively address the overestimation and underestimation of ash density derived from HU values during phantom-based densitometric calibration in high-density and low-density tissues respectively. Thus, a single relationship between  $\rho_{QCT}$  and  $\rho_{ash}$  was applied to the whole range of bone density, due to both convenience of applicability and to the higher determination coefficient for pooled data compared to the one obtained for trabecular and cortical specimens separately. Concerning the relationship between  $\rho_{ash}/\rho_{app}$ , it was found out that  $\rho_{app}$  can be accurately measured for low density trabecular specimens of any size, since in this case the  $\rho_{ash}/\rho_{app}$  ratio is comparable to the one obtained for cortical bone; nonetheless, its value might be overestimated for larger high density trabecular bone,

therefore the  $\rho_{ash}$  / $\rho_{app}$  ratio was set to 0.60 for the whole density range [28]. Finally, a Poisson ration of 0.3 was established. The obtained relationships made it possible to significantly increase the correlation between experimentally measured and FE predicted strains, and to lower the RMSE and peak errors [28]. Achieving high accuracy in strain prediction is essential, as both bone tissue failure and structural failure are fundamentally driven by deformation. Consequently, it is sensible to employ a strain-based criterion not only to evaluate the risk of fracture but also to predict and localize potential fracture sites when the bone is subjected to generic loading conditions [25]. To ensure that this strain-based framework is genuinely predictive, rigorous ex vivo validation against experimental measurements on cadaveric femurs is indispensable. In practice, intact specimens are instrumented with strain gauges under physiologically relevant configurations; principal strains predicted by the model replicating the boundary conditions implemented in vitro are then compared with experimental measurements by using linear regression, and absolute and percentage error metrics [30].

#### 1.8 Aim of the thesis

The aim of this thesis was thus to construct CT-based FE models of four human cadaveric femurs, reproducing the in-vitro experimental tests previously conducted on the same specimens to compare the models' predictions with the experimental outcomes. In the experimental set up all femurs were instrumented with up to 16 triaxial strain gauges and subjected to six loading configurations that span the entire cone of the hip joint resultant force while standing, including the single leg stance configuration and the most relevant loading configuration for spontaneous fractures (8° in the frontal plane). Corresponding boundary conditions were applied to the FE models built starting from the specimens CT images. Principal strains were extracted at nodes in the same location as the strain gauges and compared with the experimental measurements obtained for each strain gauge on each femur and for all loading configurations.

#### 2 MATERIALS AND METHODS

# 2.1 Donors and bone specimens

Two couples of cadaveric paired femurs obtained from two elderly donors were selected. Below are details concerning the donors [31]:

- Donor #1: femur #2920 (right) and femur #2921 (left). Woman, dead at 72 years old, height 162 cm, weight 63 kg
- Donor #2: femur #3154 (right) and femur #3155 (left). Woman, dead at 79 years old, height 171 cm, weight 64 kg

None of the donors were affected by any musculoskeletal disease or cancer. All the femurs were X-rayed to identify possible defects and previous traumas. They were preserved for four weeks trough a 4% formalin solution, since this procedure does not remarkably affect the mechanical properties of the bones, and continuously hydrated [31].

CT dataset of all femurs were scanned with the same machine (multislice BrightSpeed, GE Medical Systems, Waukesha, WI, USA) and parameters (120kVp, 180mA, slice thickness ranging from 0.625mm to 1.250mm, slice reconstruction ranging from 0.625mm to 1.000mm). Paired femurs were scanned together [31].

Regarding femurs #2921 and #3154, the experimental data consisted of CT dataset, experimentally measured maximum and minimum principal strains and experimental positions of strain gauges. For the other femurs, the experimental location of strain gauges was not available.

# 2.2 Experimental procedure

## 2.2.1 Marking of the anatomical reference system

Each femur was marked in order to obtain an anatomical reference system following a validated procedure [32] then integrated with an internal protocol [33].

Firstly, the femur is placed on an osteometric board resting on both condyles and the lesser trochanter, and the diaphysis is aligned. Then, the Biomechanical Length (BL), which is defined as the distance between the trochanteric fossa and the intercondylar fossa [34], is measured with a ruler. The experimental BLs for femurs #2920, #2921, #3154, and #3155 are the following [31]:

- Femur #2920: 427 mm

- Femur #2921: 427 mm

- Femur #3154: 415 mm

- Femur #3155: 412 mm

The diameter of the head (HD) is also computed as an average of five different measurements along five different directions. The experimental HDs for femurs #2920, #2921, #3154, and #3155 are the following [31]:

- Femur #2920: 47.5 mm

- Femur #2921: 47.5 mm

- Femur #3154: 46.5 mm

- Femur #3155: 47.8 mm

For cadaveric femora the two landmarks on the anterior side of the femur must be found at the two flat regions just below the lesser trochanter and above the intercondylar fossa. At both levels, the width of the diaphysis is measured and the two midpoints subsequently marked [33].

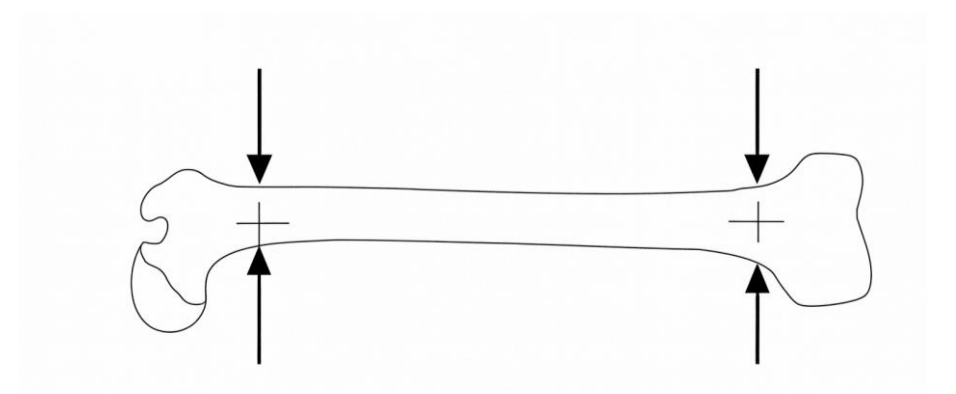


Figure 2.2-1. Left femur with the anterior side up, the location of the two landmarks is shown. Credits to [33].

The femur is then inserted into a clamping ring, with both condyles in contact with the plate. By keeping the distal end blocked, the height of the proximal end is adjusted until the two landmarks are horizontal. Once this alignment is achieved, a line is drawn connecting the two marked points, and the sagittal plane is delineated accordingly.

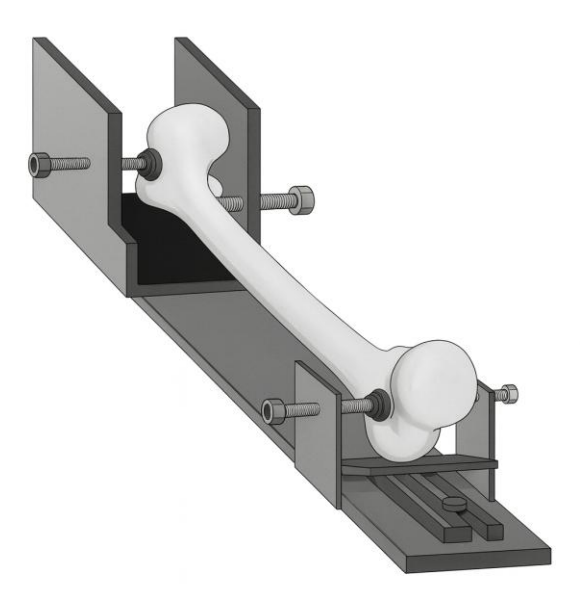


Figure 2.2-2. Femur in the clamping ring to mark the sagittal plane. Both condyles must contact the plate. Credits to [33].

The femur is then held in the same position, and the anterior-posterior width is measured at the same two levels. The femur is then placed on level surface, supported by the clamping ring, and the two midpoints on the medial side of the femur are subsequently marked and made horizontal. Finally, another line is traced to mark the frontal plane.



Figure 2.2-3. Left femur placed on a level surface supported by the clamping ring to mark the sagittal plane. Credits to [33].

# 2.2.2 Strain Gauges Placement

Each femur was instrumented with up to 16 triaxial-strain gauges (KFG-1-120-D17-23L3M2S, Kyowa, Tokyo, Japan, grid length 1/4 1mm) [31] following a validated procedure [34]:

- Four around the head (AH, LH, PH, MH), close to the articular cartilage (AH on the anterior side; LH on the lateral side; PH on the posterior side; MH on the medial side)
- Four around the neck (AN, LN, PN, MN), distal to the previous gauges (AN on the anterior side; LN on the lateral side; PN on the posterior side; MN on the medial side)
- Four around the proximal diaphysis (A0, L0, P0, M0), just below the lesser trochanter (A0 on the anterior side; L0 on the lateral side; P0 on the posterior side; M0 on the medial side)
- Four around the proximal part of diaphysis (A1, L1, P1, M1), (A1 on the anterior side; L1 on the lateral side; P1 on the posterior side; M1 on the medial side)

Strain gauges MH, MN, LH, LN are placed at the midpoint in the anterior-posterior width, whereas AH and PH, and AN and PN are located at the midpoint of head and neck in the medio-lateral direction. Analogously, A0, L0, P0, M0 and A1, L1, P1, M1 correspond to the midpoints of the diaphysis at the designated level [34].

To acquire comparable strain gauges positions on each specimen, the location of each of the four levels was determined based on fractions of the femur dimensions BL and HD [31].

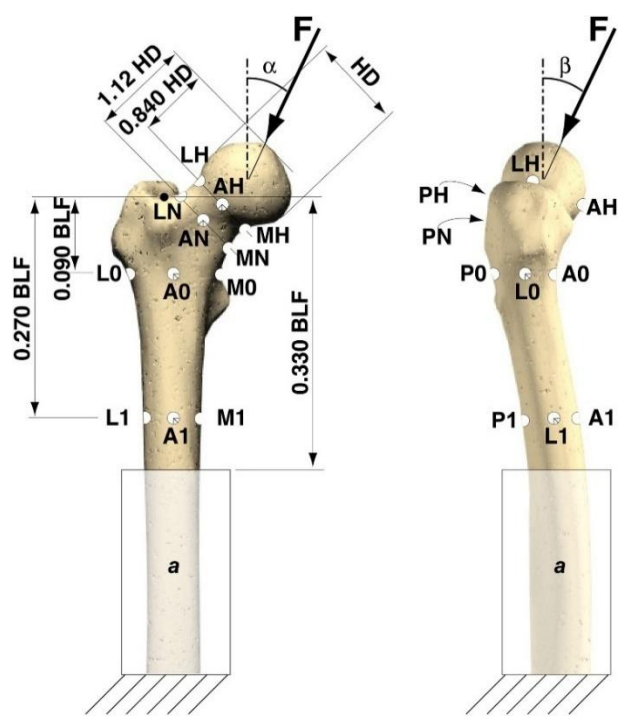


Figure 2.2-4. Proximal metaphysis of a left femur, anterior and lateral views. The position of the strain gauges based on fractions of BL and HD is shown. Credits to [35]. © Elsevier. Reproduced with permission.

To delineate the reference levels on the femoral head and neck, the femoral diaphysis was inclined at 45° in the frontal plane, with the neck anteversion adjusted to achieve a neck axis perpendicular to the ground. Conversely, to establish levels on the proximal metaphysis and diaphysis, the femoral diaphysis was positioned vertically. Starting from the intertrochanteric fossa, measurements were taken downward along the diaphysis at the established distances [36].

## 2.2.3 Loading scenario

In order to examine the strain distribution in the femur, six simplified loading configurations were designed, all of them consisting of a single force applied to the femoral head at different directions. The first four loading configurations (LC1-LC4) were thought to span the entire cone of the hip resultant force to physiological loading in the normal and sagittal plane during a variety of daily activities; thus, they do not correspond to any specific motor task. The fifth loading configuration (LC5) is thought to replicate a single leg stance condition, where the hip resultant force is applied along the diaphysis. The sixth loading configuration (LC6) consists of a force applied at 8° in the frontal plane, since this is the scenario that has been demonstrated to be more relevant for spontaneous fractures [34]. All loading configurations are applied with the intent of replicating quasi-static loading events. Muscle forces were not simulated, for it has been shown that they do not significantly affect the strain distribution in the proximal femoral metaphysis [34].

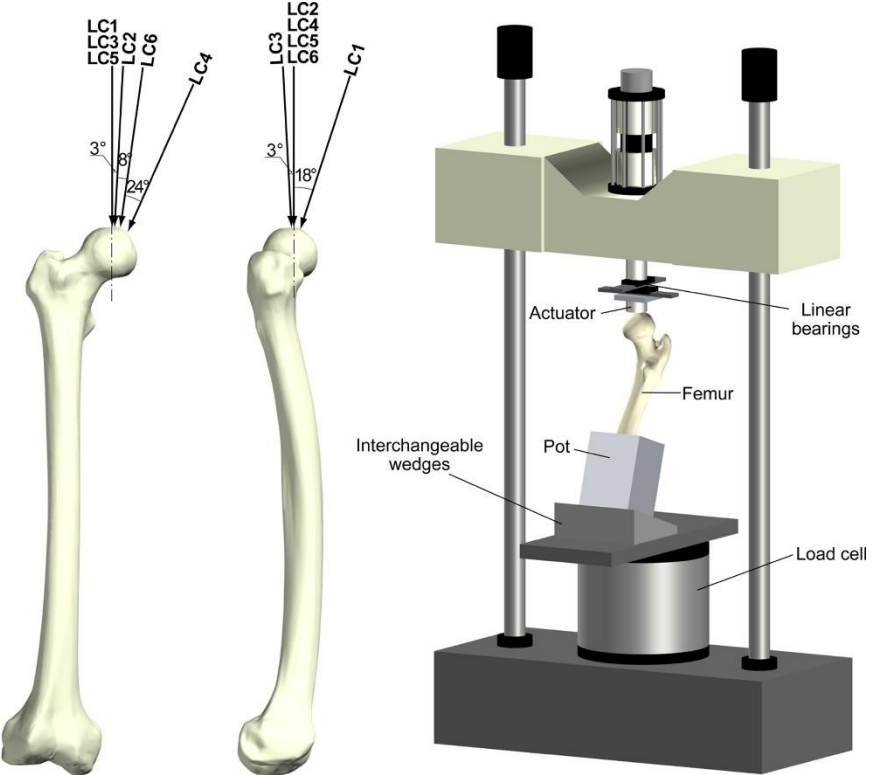


Figure 2.2-5. Anterior and lateral views of a right femur. The direction of the hip joint force for the six different loading configurations is shown, both in the frontal and in the sagittal plane. LC1-LC4 cover the extreme angle of the hip resultant force in the normal, and sagittal plane; LC5 is applied parallel to the femoral diaphysis; LC6 is tilted of 8° in the frontal plane to replicate the most relevant condition for spontaneous fractures. Credits to [17], © Elsevier. Reproduced with permission.

The directions of the six loading configurations are summarized in Table 2.2-1, where the angles they form in the frontal and sagittal planes with respect to the femoral diaphysis (considered as the vertical axis), are called  $\alpha$  and  $\beta$  respectively, as shown in Figure 2.2-5. The same figure depicts the testing apparatus on which the femurs were mounted: a platform located above the load cell that permits independent adjustment of tilt in the frontal and sagittal planes [34]. Each loading configuration was tested five times, giving the femur adequate rest between two consecutive tests.

LOADING	α	β
CONFIGURATION		
LC1 (Max flexion)	0°	+18°
LC2 (Max abduction)	+3°	0°
LC3 (Max extension)	0°	-3°
LC4 (Max adduction)	+24°	0°
LC5 (Neutral)	0°	0°
LC6 (Simulated Failure)	+8°	0°

Table 2.2-1. Directions of the six loading configuration with respect to the vertical axis in the frontal ( $\alpha$ ) and sagittal ( $\beta$ ) plane.

# 2.3 Subject-Specific CT-based FE model

## 2.3.1 Segmentation

All femurs were CT-scanned to correctly reconstruct the bone surfaces and to acquire information about density [31].

The DICOM files containing the CT scans were subsequently imported into 3D Slicer for segmentation. Each femur was segmented manually and then smoothed with a Gaussian method and a standard deviation of 2.5 mm, resulting in separate STL files for each specimen.

In femurs #3154 and #3155, that were scanned together, a slice is missing due to an error in the slice reconstruction during the acquisition of the CT dataset. The missing slice is partially reconstructed through the smoothing process, as shown in Figure 2.3-1.

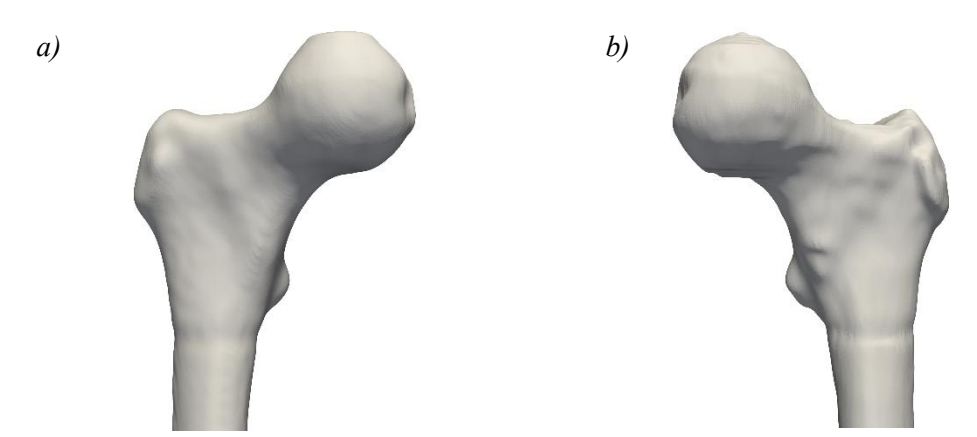


Figure 2.3-1. Segmentation of femurs #3154 (a) and #3155 (b) imported into Paraview to highlight the partial reconstruction of the missing slice, which appears as a slight necking in the metaphyseal region.

Prominent anatomical features of the femurs, such as the lesser trochanter, both condyles, the intercondylar and trochanteric fossae, as well as the flat regions located below the lesser trochanter

and above the intercondylar fossa, were identified in 3D Slicer. The three-dimensional coordinates of each point were subsequently recorded and saved in FCSV format.

These STL files, representing point cloud of the femoral surfaces, and the coordinates of the significant anatomical features, were then imported into MATLAB.

# 2.3.2 CT Reference System

Since the experimental coordinates of the strain gauges were available only for femurs #3154 and #2921, the MATLAB workflow was developed with the objective to position the computational strain gauges on femurs #3154 and #2921 as close as possible to their experimental locations. Successively, it was applied to femurs ##2920 and #3155 as for these two the experimental strain gauges positions were not available.

Therefore, experimental coordinates in mm of strain gauges placed on femurs #3154 (Table 2.3-1) and #2921 (Table 2.3-2) were also imported in MATLAB.

#3154	X	Y	${f z}$
A1	29.43	5.08	-578.52
A3	21.28	-3.53	-504.63
AH	7.01	21.14	-607.43
AN	20.18	13.88	-599.44
L3	38.42	-12.41	-505.08
LH	23.40	25.42	-623.76
LN	35.56	9.19	-615.70
M3	32.49	13.40	-504.54
MH	13.10	38.61	-593.33
MN	19.11	31.31	-587.51
P1	57.88	15.18	-576.68
PH	34.22	42.61	-608.81
PN	35.78	32.88	-599.91

Table 2.3-1. Experimental coordinates (in mm) of the strain gauges of femur #3154 (Donor #2) referred to the CT reference system.

#2921	X	Y	${f Z}$
A1	-73.06	-12.92	-175.91
A3	-76.86	-14.83	-106.57
AH	-53.63	-26.67	-202.21
AN	-64.08	-21.09	-197.76
LN	-91.76	-0.05	-162.75
L3	-88.93	-1.76	-104.77
LH	-61.67	-10.13	-218.06
M1	-50.83	5.64	-176.59
M3	-61.80	-0.21	-105.65
MH	-39.59	-8.06	-197.64
MN	-47.22	-5.65	-186.57
P1	-77.24	22.05	-174.88
PH	-45.42	2.29	-205.61
PN	-53.70	4.24	-199.19

Table 2.3-2. Experimental coordinates in mm of the strain gauges of femur #2921 (Donor #1) referred to the CT reference system.

The STL file and the coordinates of both remarkable points and experimental strain gauges were imported into MATLAB according to the CT reference system. Because of a change in nomenclature over the years, the strain gauges called A1, P1, and A3, L3, M3 in Tab 2.3-1 are referenced in literature as A0, P0, and A1, L1, M1 respectively, as reported in Figure 2.2-4. From Tables 2.3-1 and 2.3-2 is also possible to notice how not all the 16 triaxial strain gauges have been placed on femur #3154 or #2921; indeed, it is not possible to always place all the strain gauges on the femurs because of small defects on their surface or, as oftentimes happen on the lateral side of the neck, lack of space [34]. Furthermore, defects on bone surface may lead to a different placement of strain gauges compared to their nominal position up to 4 mm [34].

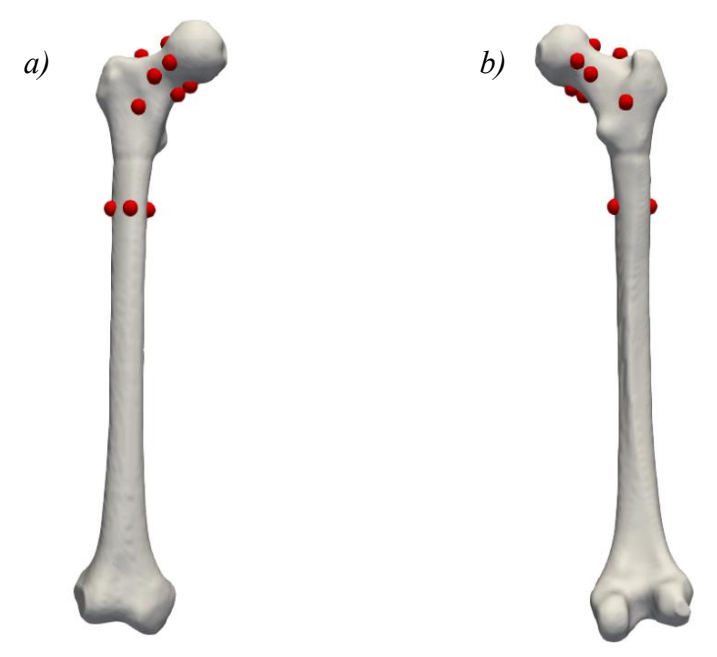


Figure 2.3-2. Experimental strain gauges placed on femur #3154 (Donor#2 right femur) after importing the point cloud in the STL file in MATLAB. a) anterior view; b) posterior view. The coordinates of the experimental strain gauges reported in Table 2.3-1 are referred to the CT reference system.

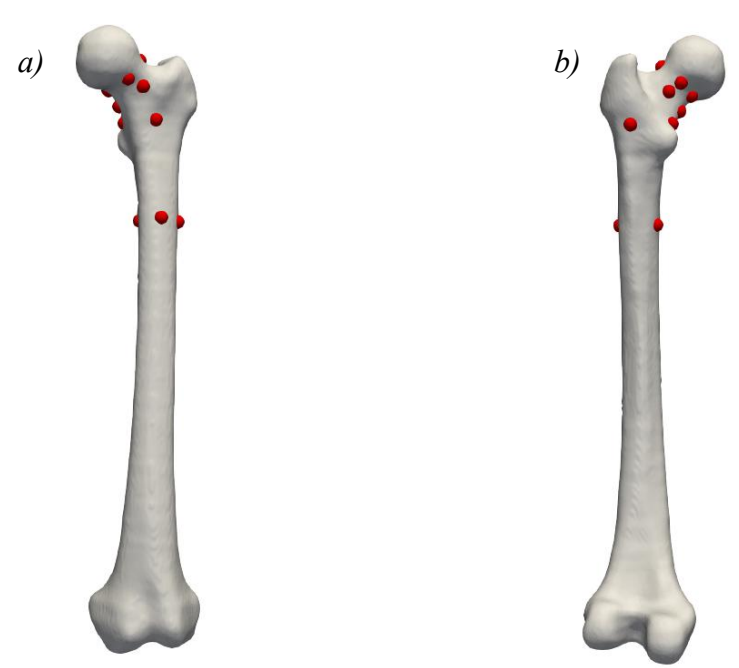


Figure 2.3-3. Experimental strain gauges placed on femur #2921 (Donor#1 left femur) after importing the point cloud in the STL file in MATLAB. a) anterior view; b) posterior view. The coordinates of the experimental strain gauges reported in Table 2.3-2 are referred to the CT reference system.

# 2.3.3 Definition of the anatomical reference system

The experimental protocol [33] was initially applied exclusively to femurs #2921 and #3154, as the experimental coordinates of the strain gauges were available only for these specimens. All subsequent images refer to femur #3154.

A plane passing through the two condyles and the lesser trochanter has been defined, so that the femur rests anterior side up.

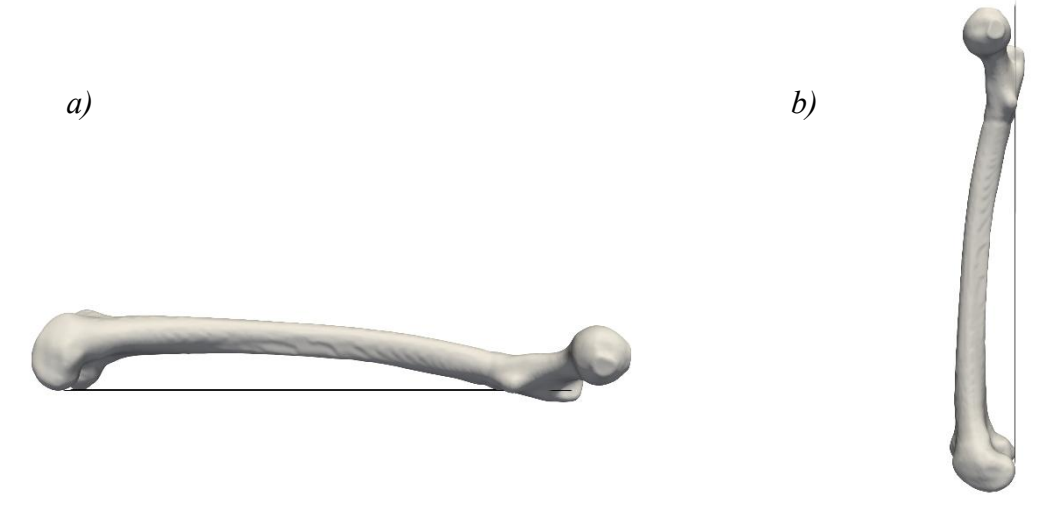


Figure 2.3-4. Femur #3154 (Donor#2 right femur) resting anterior side up on a plane defined by the lesser trochanter and the two condyles. a) lateral view, b) medial view.

A new local reference system is defined as follows:

- The origin is set in the medial condyle.
- The X-axis is defined by the vector connecting the two condyles.
- The Y-axis is normal to the plane.
- The Z-axis is determined as the cross product of the X-axis and Y-axis.

The diaphyseal axis is then aligned along the Z-axis and the BL is measured as the difference along the Z-coordinate of the intertrochanteric fossa and the intercondylar fossa [36]. The obtained value of BL for femur #3154 is 412.15 mm. Then, the widths at the two flat regions below the lesser trochanter and above the intercondylar fossa are measured. The two midpoints on the anterior side of the femur, which will be called Landmark1 and Landmark2, are pinpointed.

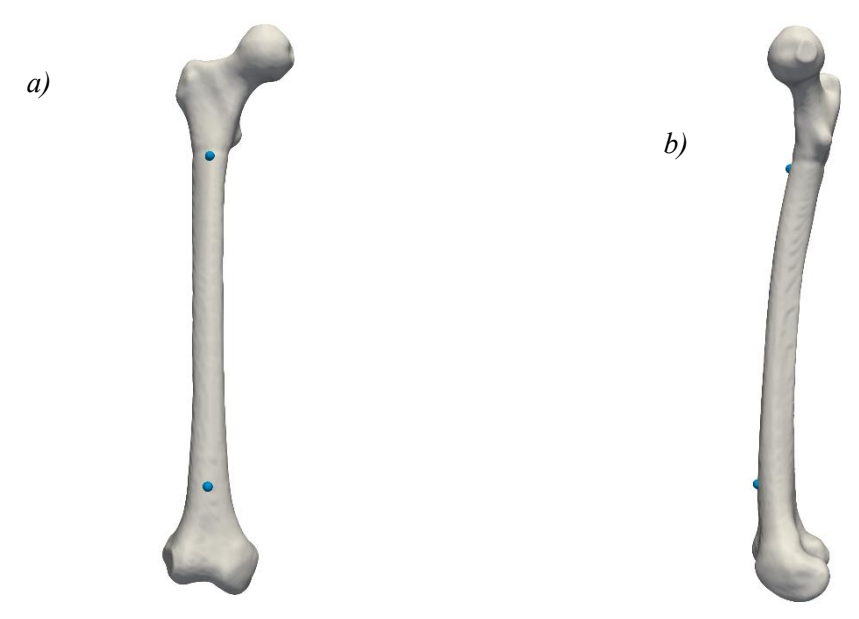


Figure 2.3-5. Femur #3154 (Donor#2 right femur), preparing for marking of the sagittal plane. The two landmarks on the anterior side are found as midthicknesses at the level of the flat regions just below the lesser trochanter and above the intercondylar fossa respectively. a) anterior side view, b) medial side view.

The femur is then rotated so that two landmarks on the anterior side are made horizontal and, subsequently, the femur is rotated again to align them vertically as well to mark the sagittal plane.

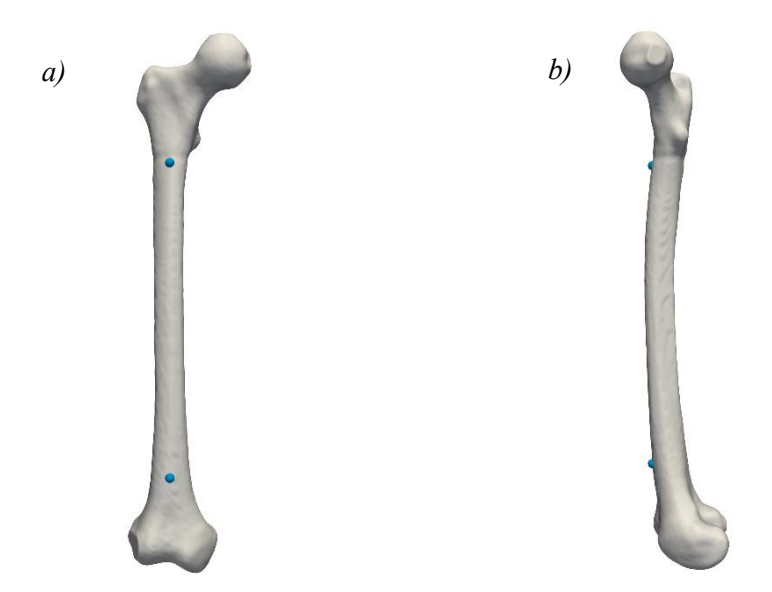


Figure 2.3-6. Femur #3154 (Donor#2 Right femur), marking of the sagittal plane. a) The two landmarks on the anterior side are made horizontal by rotating the femur; b) The two landmarks are then aligned vertically as well.

In order to mark the frontal plane as well, the midpoints are also identified at the medial side of the femur. The anterior-posterior width is measured at the same levels as before and the two midpoints, which will be called Landmark3 and Landmark4, are marked on the medial side.



Figure 2.3-7. Femur #3154 (Donor#2 right femur), preparing for marking of the frontal plane. The two landmarks on the medial side are found as midthicknesses of the anterior-posterior widths at the same two levels as before.

The femur is rotated so that the two landmarks on the medial side are made horizontal.



Figure 2.3-8. Femur #3154 (Donor#2 right femur), marking of the frontal plane. The two landmarks on the medial side made horizontal.

Therefore, a new anatomical reference system based on the defined frontal and sagittal plane is set. Finally, the HD is measured by using a spherical fitting of the head of the femur. The obtained HD for femur #3154 is 45.8 mm.

# 2.3.4 Identification the strain gauges positions on MATLAB

The aim of this part of the project is the positioning of the strain gauges in MATLAB on the point cloud of the femur following the experimental protocol [34], [37], so that their positions match the experimental ones. The initial coordinates of the experimental strain gauges reported in Table 2.3-1 and in Table 2.3-2 changed accordingly to the translation and rotations the femur was subjected to.

Firstly, after the definition of the frontal and sagittal plane, strain gauges A0, P0, and A1, L1 and M1 were positioned along the metaphysis and diaphysis of the femur, starting from the intertrochanteric fossa and extending vertically over the predetermined distance of 0.90BLF and 0.270BLF respectively [17], [31], [35] as shown in Figure 2.3-9. To place strain gauges on the lateral and medial side (strain gauges "L" and "M") in correspondence of the frontal plane [34], the width of the femur at said levels were measured in the anterior-posterior direction and the midpoint was marked; analogously, to place strain gauges on the anterior and posterior side (strain gauges "A" and "P") the width of the femur was measured on the medial- lateral direction and the midpoint was identified [37]. To achieve this, a vertical line was first traced from the intertrochanteric fossa up to the predetermined height. A plane perpendicular to this vertical axis was then defined, and its intersection with the femoral point cloud was computed. The resulting intersection points were fitted with a

polyline representing the cross-sectional contour of the femur at that level. The width in the frontal plane was subsequently measured as the distance between the two most laterally separated points of the diaphyseal contour in the frontal plane. The midpoint of this width was identified and used to trace a second line along the anterior-posterior direction, intersecting the polyline at the anterior and posterior extents of the femoral point cloud. Strain gauges "A" and "P" were then defined as the points belonging to the femur point cloud closest to the anterior and posterior intersections respectively. Strain gauges "L" and "M" were defined as the points belonging to the femur point cloud closest to the two most laterally separated points used to measure the width in the frontal plane.

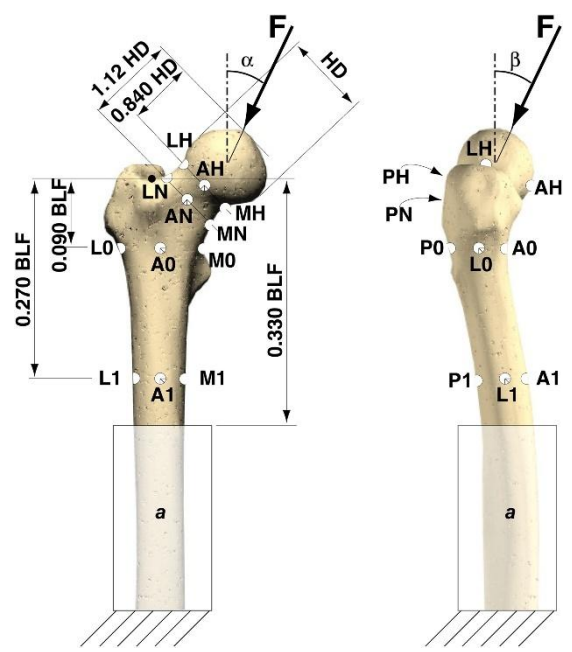


Figure 2.3-9. Proximal metaphysis of a left femur, anterior and lateral views. The position of the strain gauges A0, P0 on the metaphysis and of strain gauges A1, L1, M1 on the metaphysis is depicted. Credits to [35]. © Elsevier.

Reproduced with permission.

For femur #3154, the resulting distances between the experimental and computational strain gauges, together with the corresponding images of all strain gauges organized by level, are reported as follows:

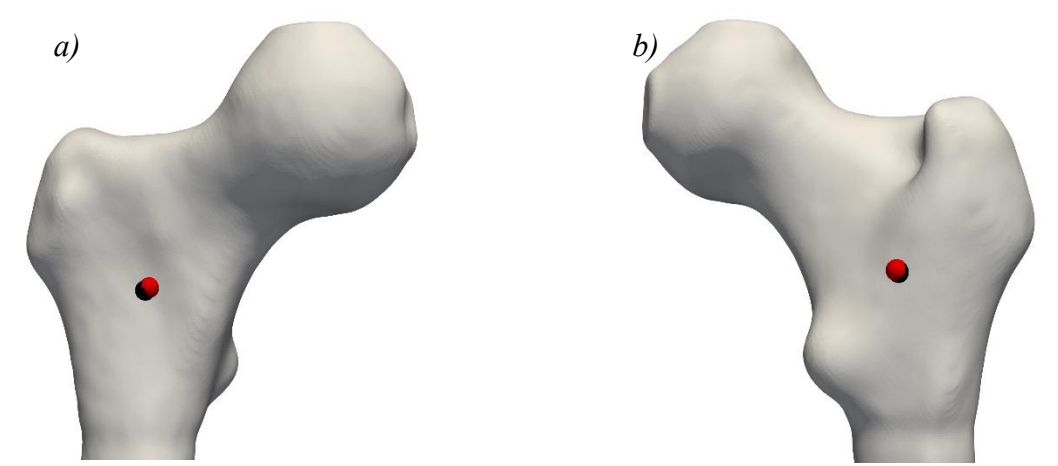


Figure 2.3-10. Femur #3154. Visualization of experimental strain gauge placement (in red) and computationally determined strain gauge locations (in black) for the metaphysis of the femur. Views are presented from the (a) anterior and (b) posterior sides, corresponding respectively to the positions of strain gauges A0 and P0, in order to highlight both experimental and computed placements.

	DISTANCES (mm)
A0	1.32
P0	0.65

Table 2.3-3. Distances between experimental strain gauges computationally determined strain gauges in the metaphyseal region. Distances were calculated between the strain gauges placed at level 0 and the experimental strain gauges labeled A1 and P1, reflecting the change in nomenclature as previously described.

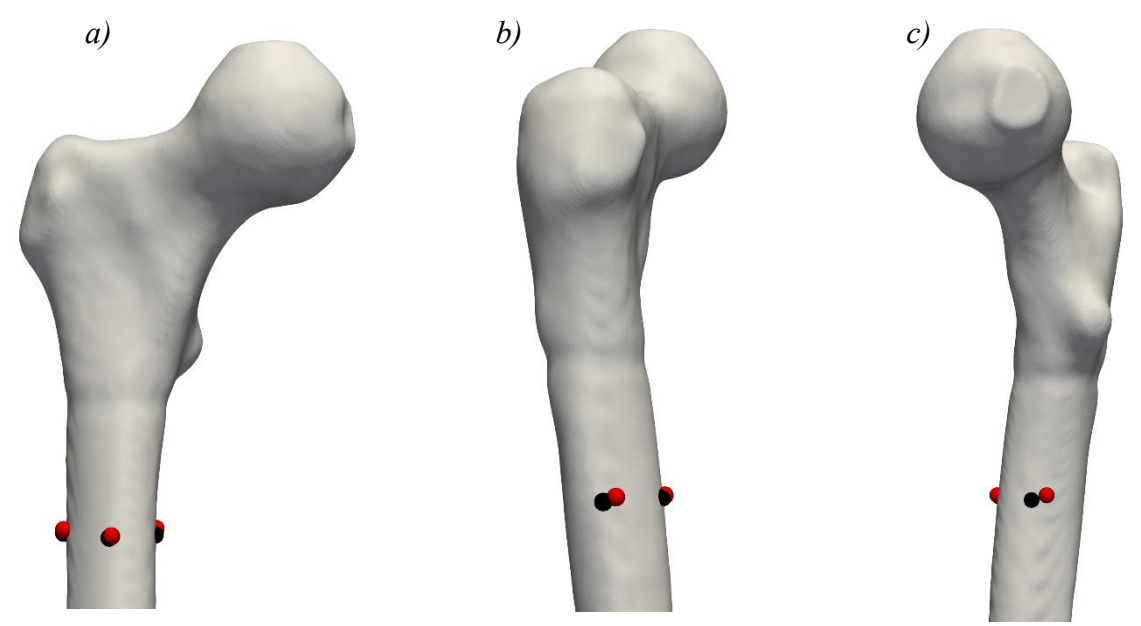


Figure 2.3-11 Femur #3154. Visualization of experimental strain gauge placement (in red) and computationally determined strain gauge locations (in black) for the diaphysis region of the femur. Views are presented from the (a) anterior, (b) lateral, and (c) medial sides, corresponding respectively to the positions of strain gauges A1, L1, and M1, in order to highlight both experimental and computed placements.

	DISTANCES (mm)
A1	0.91
L1	3.62
M1	4.78

Table 2.3-4. Distances between experimental strain gauges computationally determined strain gauges in the metaphysis region. Distances were calculated between the strain gauges placed at level 1 and the experimental strain gauges labeled A3, L3, and P3, reflecting the change in nomenclature as previously described.

With regard to the head and neck region, as reported in [36], once the frontal and sagittal planes were established, the femoral point cloud was initially rotated to compensate for the anteversion of the neck. The region corresponding to the femoral neck was first manually isolated on the point cloud, and the anatomical neck axis was subsequently identified through an elliptical fitting

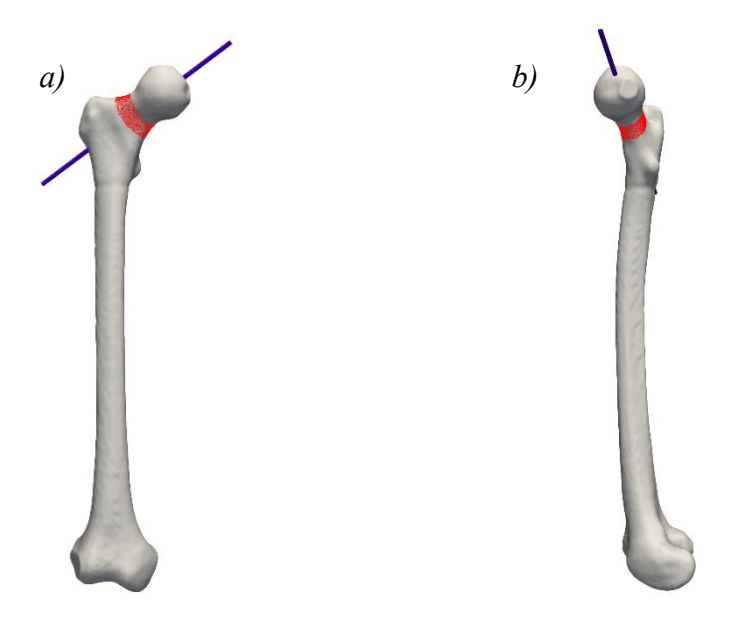


Figure 2.3-12. Femur #3154, frontal (a) and sagittal (b) plane. Isolation of the neck region (in cyan) and computation of the anatomical neck axis (in red).

A corrective rotation was then performed, aimed at aligning the anatomical neck axis with the vertical axis in the sagittal plane.

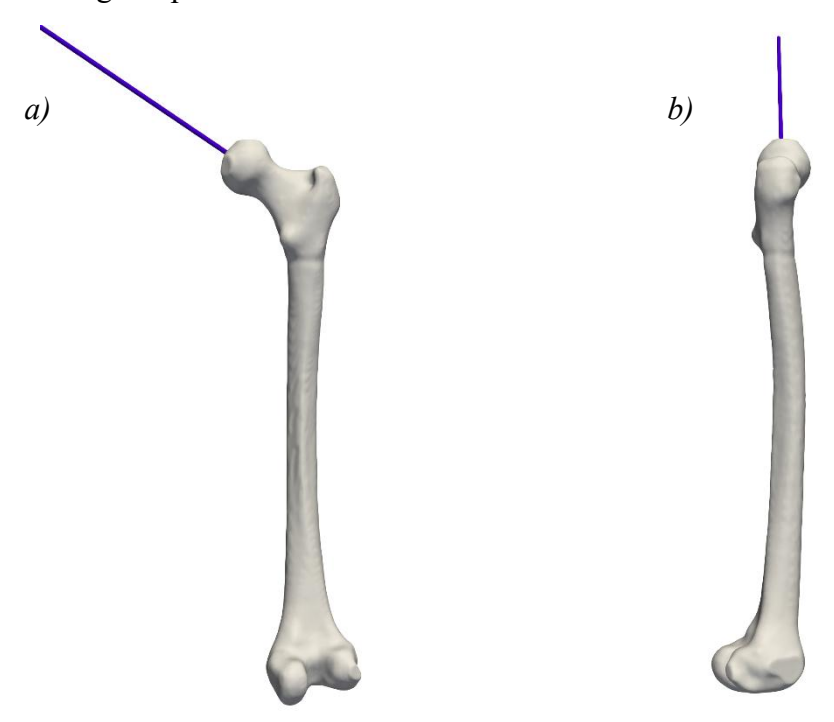


Figure 2.3-13. Femur #3154. The femur was rotated so that the neck axis (in red) could become parallel to the vertical axis of the diaphysis. The two landmarks defining the frontal plane (a) and the two landmarks defining the sagittal plane (b) are also shown.

Subsequently, the femur was rotated along the frontal plane of 45° so that the actual neck axis was perpendicular to the ground [36].

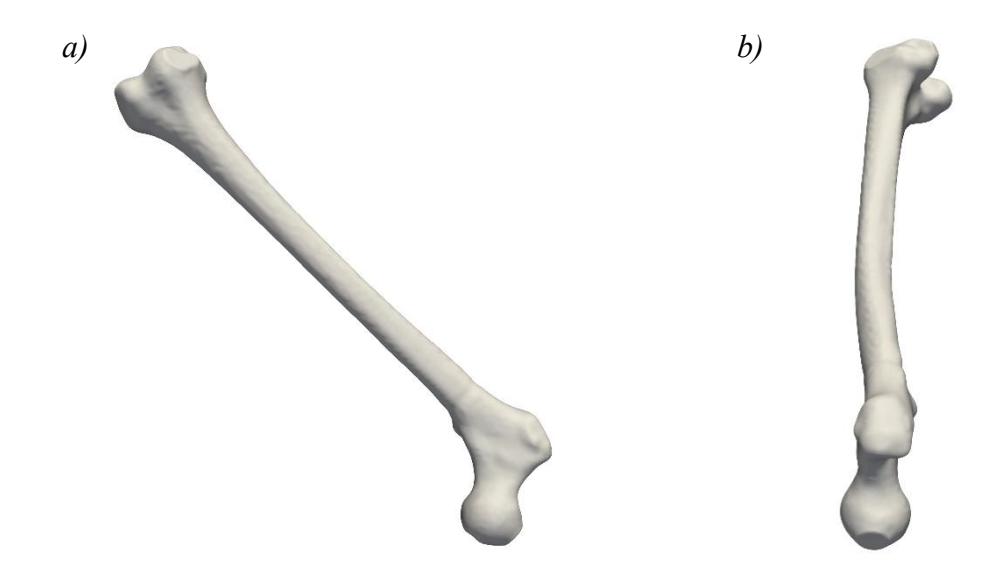


Figure 2.3-14. Femur #3154, visualized in the XZ plane (a) and YZ plane (b). The femur was rotated by 45° in the frontal plane, allowing the actual neck axis to be considered as aligned with the vertical axis, i.e., perpendicular to the ground.

Strain gauges on the head and on the neck were positioned by tracing the correspondent levels (Figure 2.3-9) at the predetermined heights of 0.84HD and 1.120HD respectively. These heights were found by tracing a line starting from the lowest point of the point cloud vertically, namely along the actual neck axis. Strain gauges LH, LN, MH, MN were located at the midpoint of the anterior-posterior width, at the corresponding levels; AH, AN, PH, PN were identified at the midpoint of the lateral-medial width at their established levels as well [34].

In order to do so, the same procedure previously described for the metaphysis and diaphysis has been applied for the head and neck region. A line was first traced from the point exhibiting the lowest *z*-coordinate at the predetermined levels, then a plane perpendicular to the line was generated and the intersecting points with the femur point cloud were identified. The resulting intersection points were fitted with a polyline, and the width of this polyline was measured to determine its midpoint.

From this midpoint, a second line was drawn perpendicular to the width in order to identify the two intersection points on the anterior and posterior sides of the polyline. Strain gauges labeled "A" (anterior) and "P" (posterior) were subsequently placed on the points within the femoral point cloud that were closest to these anterior and posterior intersection points, respectively. Similarly, strain

gauges "L" (lateral) and "M" (medial) were positioned on the points of the femoral point cloud nearest to the two most distal points used in the width measurement.

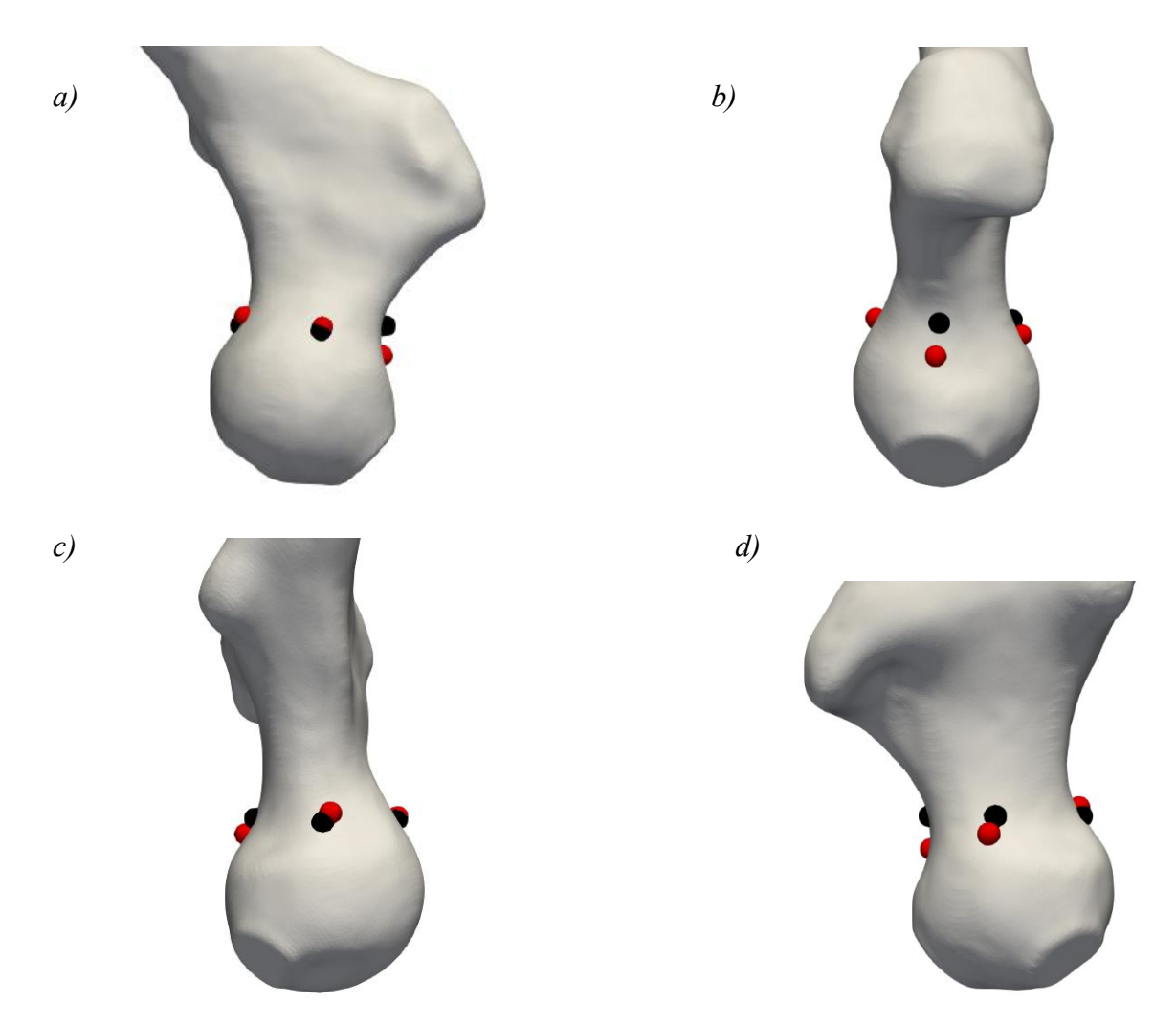


Figure 2.3-15. Femur #3154. Visualization of experimental strain gauge placement (in red) and computationally determined strain gauge locations (in black) for the head region of the femur. Views are presented from the (a) anterior, (b) lateral, (c) medial, and (d) posterior sides, corresponding respectively to the positions of strain gauges AH, LH, MH, and PH, in order to highlight both experimental and computed placements.

	DISTANCES (mm)
AH	1.01
LH	7.26
MH	2.96
PH	3.59

Table 2.3-5. Distances between experimental strain gauges and computationally determined strain gauges in the head region.

As shown in Figure 2.3-15 and reported in Table 2.3-5, the distance between the experimental and computed position of strain gauge LH is relatively large. Nonetheless, it is also evident that the experimental strain gauge was placed lower than the other strain gauges, suggesting that the elevated distance may be attributed to an incorrect (or forced by defects on the specimen) positioning.

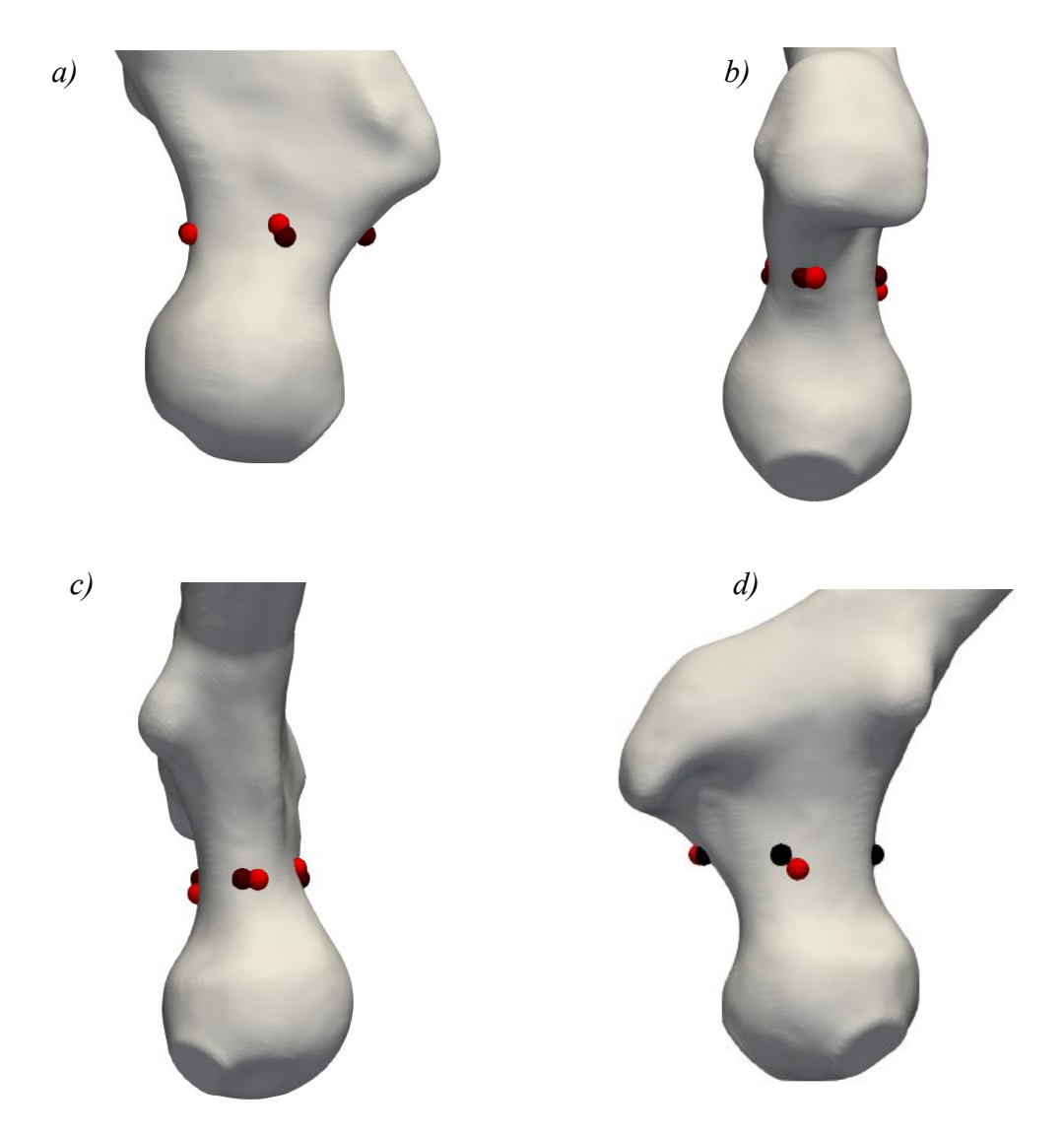


Figure 2.3-16. Femur #3154. Visualization of experimental strain gauge placement (in red) and computationally determined strain gauge locations (in black) for the neck region of the femur. Views are presented from the (a) anterior, (b) lateral, (c) medial, and (d) posterior sides, corresponding respectively to the positions of strain gauges AN, LN, MN, and PN, in order to highlight both experimental and computed placements.

	DISTANCES (mm)
AN	3.28
LN	1.39
MN	3.48
PN	4.77

Table 2.3-6. Distances between experimental strain gauges and computationally determined strain gauges in the neck region.

As already mentioned for strain gauge LH, the high distance reported for strain gauge PN in Table 2.3-6, is probably due to the incorrect or forced positioning of the experimental strain gauge lower compared to the others, as also highlighted in Figure 2.3-16.

All the distances, excluding strain gauges LH and PN (with the exception of M1, whose distance is slightly higher than the expected), are below 4 mm, which is consistent with threshold distance established between nominal and experimental positions of strain gauges [34]. Concerning M1, the distance over threshold might be due to uncertainties related to the segmentation process.

The same procedure has then been applied to femur #2921:

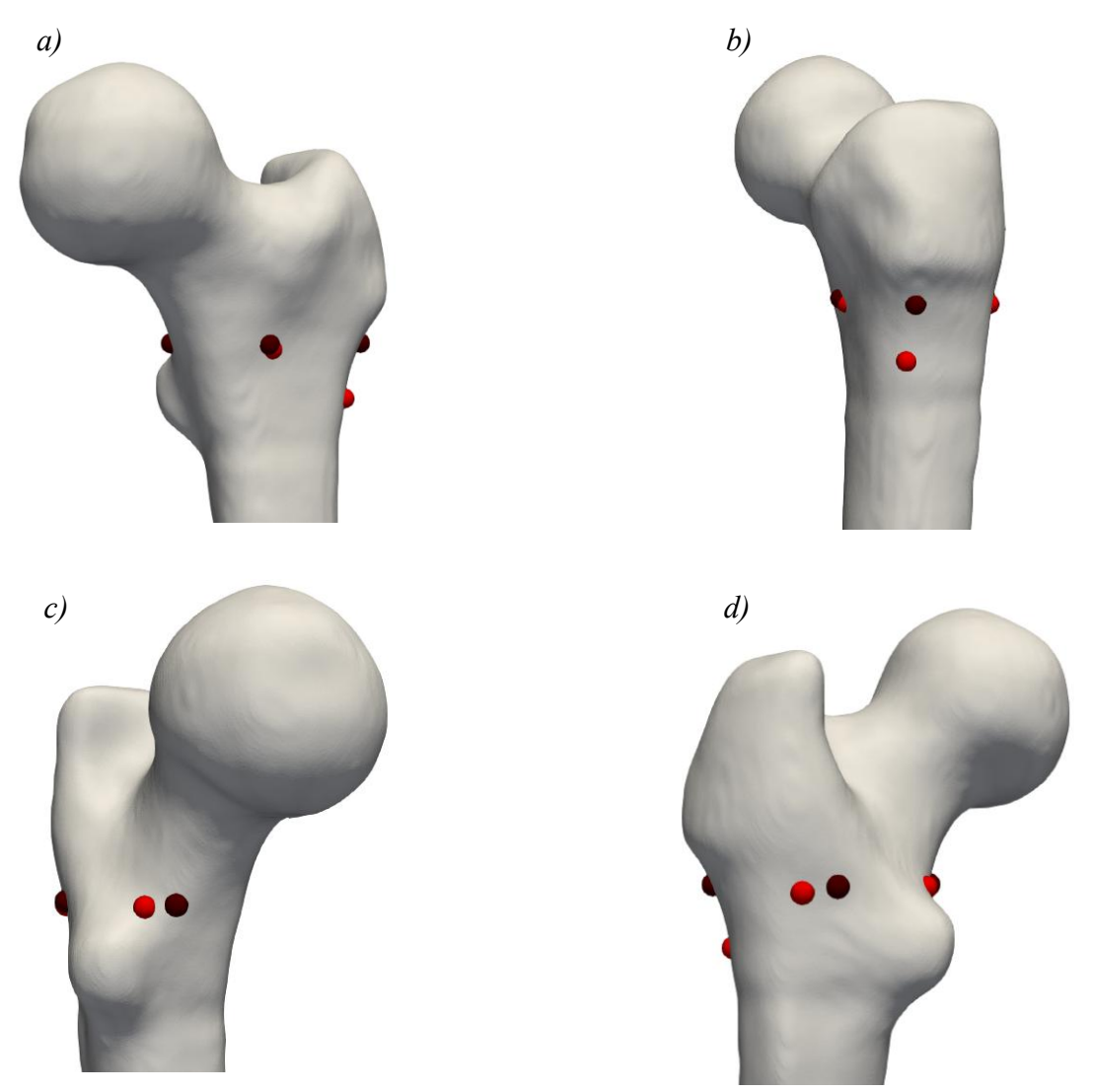


Figure 2.3-17. Femur #2921. Visualization of experimental strain gauge placement (in red) and computationally determined strain gauge locations (in black) for the metaphysis of the femur. Views are presented from the (a) anterior, (b) lateral, (c) medial, and (d) posterior sides, corresponding respectively to the positions of strain gauges A0, L0, M0, and P0, in order to highlight both experimental and computed placements.

	DISTANCES (mm)
A0	1.860
L0	14.349
M0	3.874
P0	5.924

Table 2.3-7. Distances between experimental strain gauges and computationally determined strain gauges in the metaphyseal region. Distances were calculated between the strain gauges placed at level 0 and the experimental strain gauges labeled A1, L1, M1 and P1, reflecting the change in nomenclature as previously described.

As reported in Table 2.3-7, the distance between the experimental and computed strain gauge L0 is very high; nonetheless, it is possible to observe in Figure 2.3-17 that the experimental strain gauge has been positioned much lower compared to the other strain gauges; therefore the high distance is due to an incorrect positioning of the experimental strain gauge, that might be caused by a defect in the nominal position on the cadaveric femur.

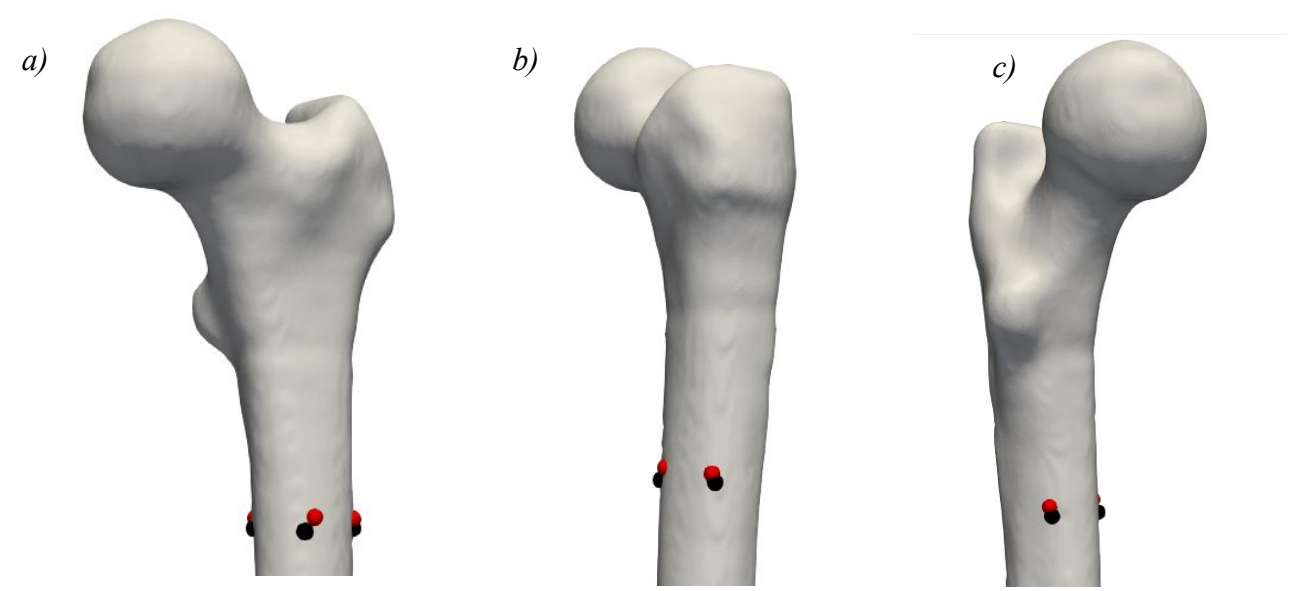


Figure 2.3-18. Femur #2921. Visualization of experimental strain gauge placement (in red) and computationally determined strain gauge locations (in black) for the proximal diaphysis of the femur. Views are presented from the (a) anterior, (b) lateral, and (c) medial sides, corresponding respectively to the positions of strain gauges A1, L1, and M1, in order to highlight both experimental and computed placements.

	DISTANCES (mm)	
A1	5.135	
L1	3.015	
M1	5.674	

Table 2.3-8. Distances between experimental strain gauges and computationally determined strain gauges in the diaphysis region. Distances were calculated between the strain gauges placed at level 1 and the experimental strain gauges labeled A3, L3, and P3, reflecting the change in nomenclature as previously described.

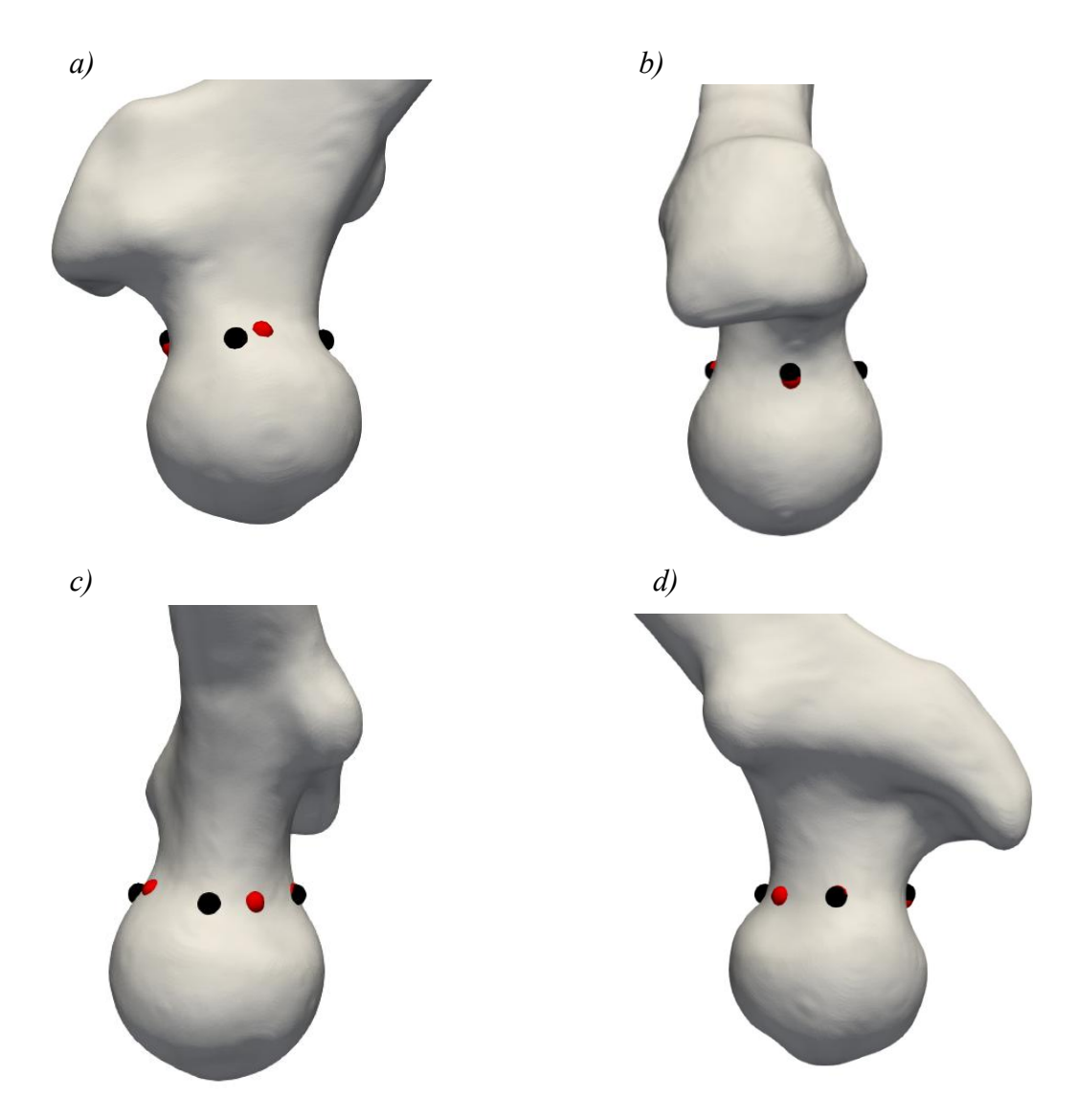


Figure 2.3-19. Femur #2921. Visualization of experimental strain gauge placement (in red) and computationally determined strain gauge locations (in black) for the head region of the femur. Views are presented from the (a) anterior, (b) lateral, (c) medial, and (d) posterior sides, corresponding respectively to the positions of strain gauges AH, LH, MH, and PH, in order to highlight both experimental and computed placements.

	DISTANCES (mm)
AH	6.291
LH	1.386
MH	9.837
PH	0.666

Table 2.3-9. Distances between experimental strain gauges and computationally determined strain gauges in the head region.

As reported in Table 2.3-9, the distance between the experimental and computed position of strain gauge MH is notably high. Nonetheless, Figure 2.3-19 shows that the experimental strain gauge was not correctly centered at the midpoint of the anterior—posterior width. Therefore, the large discrepancy can be attributed to an incorrect placement of the experimental strain gauge, likely resulting from a defect in the nominal positioning on the cadaveric femur.

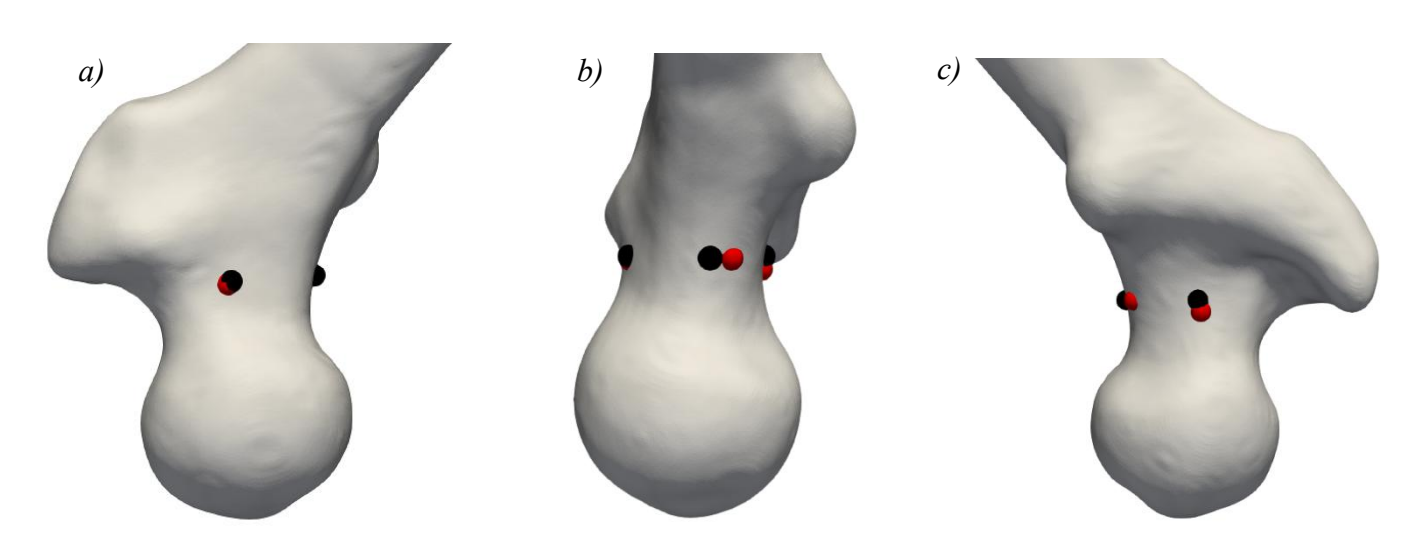


Figure 2.3-20. Femur #2921. Visualization of experimental strain gauge placement (in red) and computationally determined strain gauge locations (in black) for the neck region of the femur. Views are presented from the (a) anterior, (b) medial, and (c) posterior sides, corresponding respectively to the positions of strain gauges AN, MN, and PN, in order to highlight both experimental and computed placements.

	DISTANCES (mm)	
AN	1.057	
MN	4.542	
PN	2.878	

Table 2.3-10. Distances between experimental strain gauges and computationally determined strain gauges in the neck region.

Compared to femur #3154, femur #2921 generally presents larger distances, which, excluding strain gauges L0 and MH, reach up to 6 mm. Nonetheless, the procedure can still be considered adequate, as these higher distances are likely attributable to segmentation inaccuracies or, at the diaphyseal level (level 1), to slight differences in the measurement of the BL.

This methodology was subsequently applied to the other two femurs whose experimental strain gauges coordinates were not available.

## 2.3.5 Meshing

The coordinates of the experimental strain gauges of the two femurs for which they were available, and the coordinated of the strain gauges identified in MATLAB for the other two femora were subsequently subjected to the inverse rotations to retrieve their coordinates within the CT reference system. In the preliminary phase, the STL point cloud of the femur was imported into MeshLab, where an isotropic remeshing procedure was performed to prevent potential issues during the subsequent meshing process. The resulting femoral surface is a single, continuous component composed of triangular elements. The STL file processed in MeshLab was subsequently imported into Hypermesh 2019.



Figure 2.3-21. Before the actual meshing process in Hypermesh 2019, femur #3154 has been isotropically remeshed in MeshLab to enhance the quality of the STL obtained from 3DSlicer and prevent further complications during the realization of the 3D mesh. The resulting femoral surface is a single, continuous component composed of triangular elements.

The first step in Hypermesh 2019 involved manually entering the coordinates of each strain gauge within the CT reference system, enabling their use as anchor nodes during both the 2D and 3D meshing processes.

The 2D mesh has been generated by applying a first-order triangular mesh to the component, with an element size set to 2 mm. Subsequently, a 3D tetrahedral solid mesh was created, featuring a maximum element size of 2 mm and a growth rate of 1. The choice of 2 mm size was supported by literature, as it has been demonstrated that it provides a good compromise between computational

cost and prediction accuracy [30]. The element order of the solid mesh has been then upgraded to second order, resulting in a 10-node tetrahedral 3D mesh.

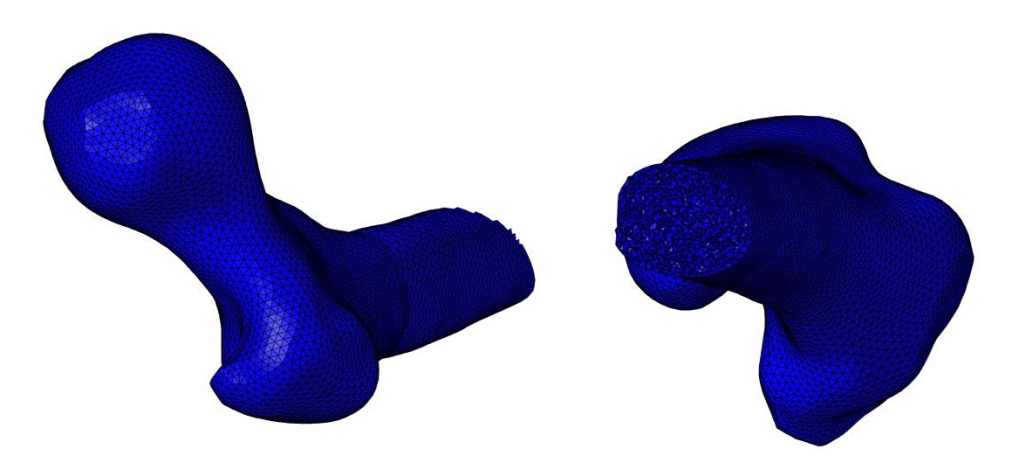


Figure 2.3-22. 10-node tetrahedral 3D mesh of femur #3154 obtained in Hypermesh 2019. The central portion of the femur has been masked to illustrate that the mesh is fully solid.

The element type has been set to SOLID187. Finally, the nodes of the 3D mesh were renumbered and the model exported with a CDB extension. The CDB file contains info about the nodes of the 3D mesh and the connectivity.

## 2.3.6 Assignment of non homogeneous material properties

The assignment of material properties to the mesh is performed using Bonemat Rolling, a in-house developed software which enables the calibration of the CT dataset. CT relies on the absorption of an X-ray beam by biological tissues, where the degree of energy absorption, or attenuation, is directly proportional to the tissue's physical density. Hounsfield Units (HU) are derived through a linear transformation of the measured attenuation coefficients, by convention assigning a radiodensity value of 0 HU to distilled water at standard temperature and pressure (STP) and -1000 HU to air under the same conditions [38]. The linear transformation generates a Hounsfield scale, a quantitative relative grey scale in which denser tissues, which absorb more energy, have higher HU and appear brighter, whereas less dense tissues, that absorb less energy, appear darker, and have lower HU. HU values are thus related to the density of the tissue but also depend on the acquisition parameters (KVP and Xray Tube Current), CT scanner, and CT artefacts [38], meaning the same specimen scanned with two different machines or with the same machine but different parameters will present different HU values. Therefore, the CT dataset must be calibrated by using a phantom scanned with the same scanning machine and the same (or as similar as possible) parameters (KVP and Xray Tube Current) as those used for the femurs. For femurs #3154, #3155, #2920, and #2921, which were scanned using a multislice BrightSpeed system (GE Medical Systems, Waukesha, WI, USA) with acquisition parameters of 120 kVp and 180 mA [31], no phantom scan acquired under identical conditions was available. Consequently, a phantom scan obtained with the same multislice BrightSpeed system and parameters of 120 kVp and 80 mA was selected for the segmentation process, as it was deemed the most comparable.

First, each insert of the phantom must be segmented separately, assigning a distinct label to each one (for example, red, green, and yellow in Fig. 2.3-23). Subsequently, by using the Segment *Statistics* tool, it is possible to compute the mean Hounsfield Unit (HU) value for each "vertebra" of the phantom. The three vertebrae correspond, in order of increasing brightness—and thus increasing density—to the spinous process, cancellous bone, and cortical bone [29]. Their known hydroxyapatite (HA) densities are, respectively,0.0505  $\frac{g[HA]}{cm^3}$ , 0.1013  $\frac{g[HA]}{cm^3}$ , 0.1981  $\frac{g[HA]}{cm^3}$ .

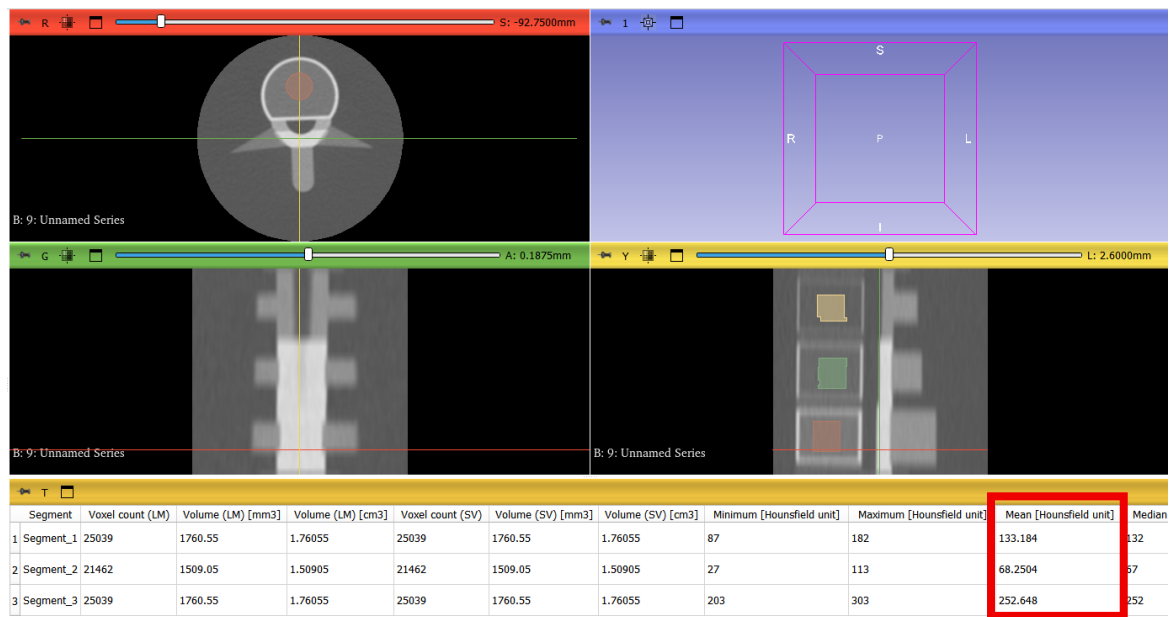


Figure 2.3-23. Segmentation of the phantom used to calibrate the CT dataset for all femurs. Three separate segmentations were performed for the inserts representing the spinal process, cancellous bone, and cortical bone, shown in yellow, green, and red, respectively. Using the Segment Statistics tool, the mean HU value for each insert was obtained (highlighted in the red box in the figure), showing an increase in HU corresponding to increasing insert density.

Based on the mean HU values obtained, the corresponding HU–density relationship was determined through linear regression, yielding the following regression equation:

$$\rho_{OCT} = a + b * HU$$

Where a and b represent the intercept and the slope computed by the calibration respectively.

For all femurs the three mean HU values obtained for the spinal process, cancellous bone, and cortical bone are 68.2504, 133.184, and 252.648, respectively.

The regression line is here reported:

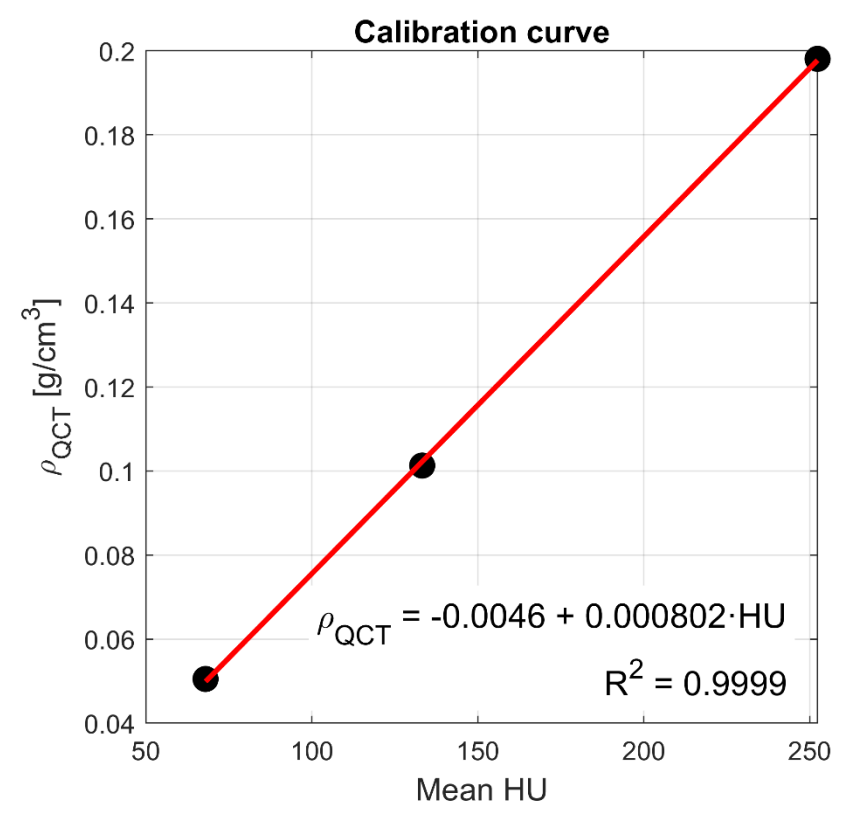


Figure 2.3-24 Regression line for femurs #2920, #2921, #3154, #3155

As reported in Figure 2.3-24, the regression line derived from phantom calibration is:

$$\rho_{QCT} = 0.008 * HU - 0.0046 \tag{1}$$

These regression equations were implemented in Bonemat Rolling to calibrate the CT datasets. In this process, the DICOM images containing the CT scan and the 3D finite element mesh exported from HyperMesh are imported and visualized together in Bonemat Rolling (Figure 2.3-25).

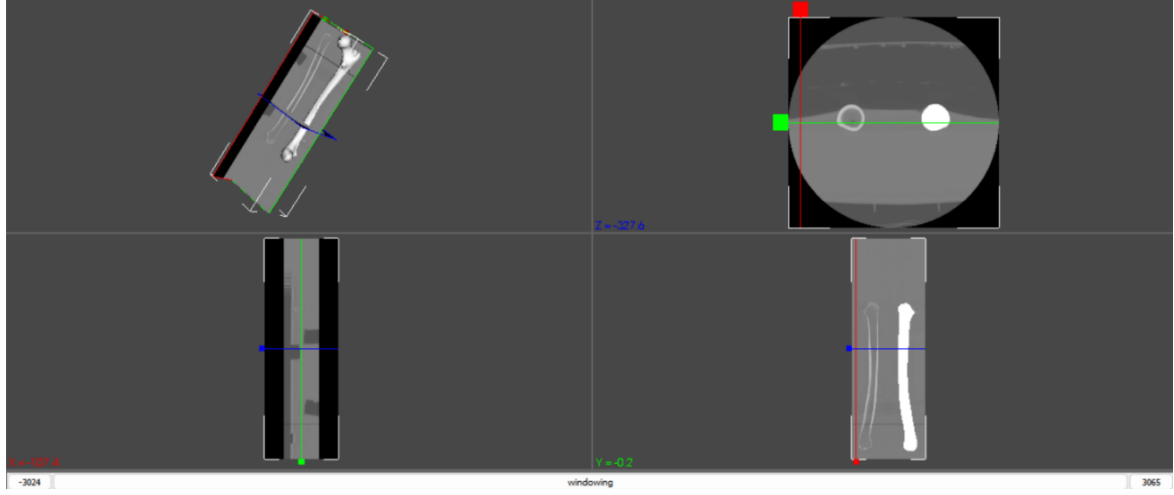


Figure 2.3-25. The 3D mesh for femur #3154 has been imported into Bonemat Rolling and visualized.

Within Bonemat Rolling, by selecting the mesh and applying the  $Operations \rightarrow Bonemat$  function, non-homogeneous, yet locally isotropic, mechanical properties are assigned to the mesh elements. It is essential that the mesh is precisely registered and perfectly overlapped with the DICOM images to ensure correct mapping.

The first equation applied is Equation (1) to convert HU values to calibrated quantitative CT density  $\rho_{OCT}$ .

The second equation corrects the phantom-based densitometric calibration to compensate for the tendency to overestimate  $\rho_{ash}$  in high-density tissues and underestimate it in low-density tissues [28].

$$\rho_{ash} = a + b * \rho_{QCT} \tag{2}$$

The third equation converts  $\rho_{ash}$  into  $\rho_{app}$ :

$$\rho_{ash} = a * \rho_{app} \quad \text{, where } a = 0.60$$
 (3)

Finally, Young's modulus E is computed according to:

$$E = a + b * \rho^c \tag{4}$$

Where a=0, b=14664, and c=1.49. In this thesis,  $\rho = \rho_{ash}$ .

Through the application of these four equations, each voxel HU value can be converted into a corresponding voxel-based E value. The resulting elastic modulus field is then averaged over the elements of the finite element mesh. This voxel-wise conversion followed by element-wise averaging has been shown to yield higher predictive accuracy than the alternative approach of first averaging HU values within each element and subsequently converting the mean HU into an average E value [27], as already highlighted in Section 2.4.

Equations (2), (3), and (4) are taken from the literature; in particular, Equation (4) is based on the density—elastic modulus relationship proposed by Morgan et al., 2003 [24], which has been shown to provide the highest predictive accuracy for strain estimation in CT-based, subject-specific finite element models of bones [17]. The output of this process is a new ANSYS .CDB file containing not only the nodal coordinates and element connectivity of the 3D mesh, but also the assigned material properties. Each element is assigned a specific value of E, resulting in a bone model with spatially varying (non-homogeneous) but locally isotropic mechanical properties, as shown in Figure 2.3-26.

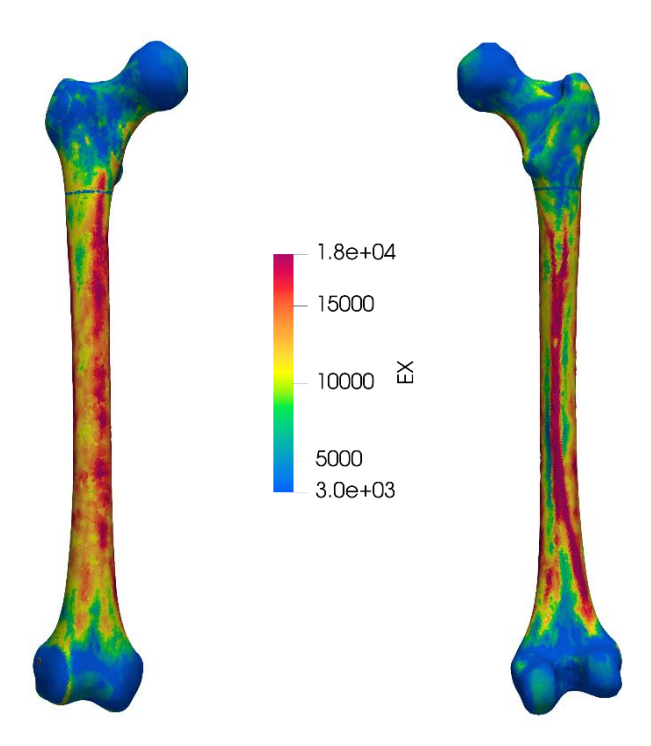


Figure 2.3-26. Femur #3154. ANSYS .CDB file generated with Bonemat Rolling for femur #3154, imported into Paraview to visualize the spatial distribution of the material properties assigned to each finite element.

For each femur, the CDB file containing the nodal coordinates and material properties was imported into MATLAB and processed with the same pipeline developed for femur #2921 and femur #3154; in particular, the nodes of the mesh were treated as the femur point cloud. In this part of the project, the aim was to rotate the mesh in order to represent the six simplified loading configurations here recalled in the table below (Table 2.3-11).

LOADING	α	β
CONFIGURATION		
LC1 (Max flexion)	0°	+18°
LC2 (Max abduction)	+3°	0°
LC3 (Max extension)	0°	-3°
LC4 (Max adduction)	+24°	0°
LC5 (Neutral)	0°	0°
LC6 (Simulated Failure)	+8°	0°

Table 2.3-11. Directions of the six loading configuration with respect to the vertical axis in the frontal ( $\alpha$ ) and sagittal ( $\beta$ ) plane.

After aligning the nodes to the anatomical reference system defined in [33], the mesh is in the neutral position (LC5). The mesh is then rigidly rotated to generate the remaining five configurations (LC1–LC4 and LC6), thereby obtaining the nodal coordinates corresponding to the six simplified loading states.

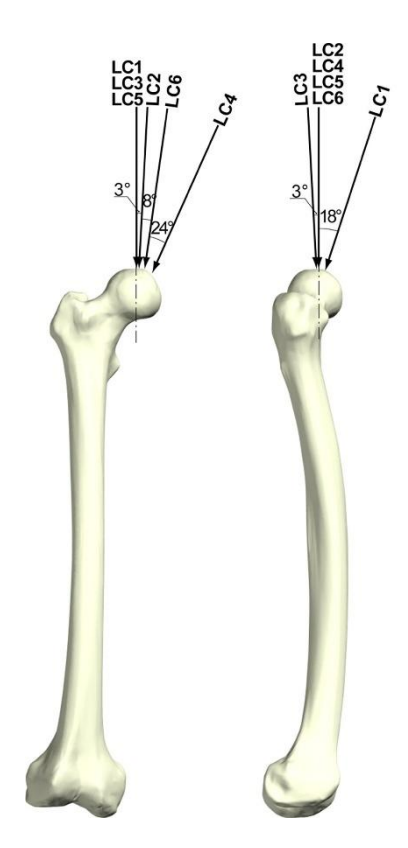


Figure 2.3-27. The six loading configurations, shown as a single force directed onto the head of the femur at different inclinations, are here represented on a right femur. Credits to [17]. © Elsevier. Reproduced with permission

As shown in Figure 2.3-27, LC2, LC4, and LC6 require a rotation in the frontal plane, represented in the figure by the angle  $\alpha$ , whereas LC1 and LC5 require a rotation in the sagittal plane, represented by the angle  $\beta$ .

For each femur and for each loading configuration (including the neutral condition), the rotated nodal coordinates are written back to the Bonemat-generated CDB by replacing the original CT-frame coordinates of the corresponding nodes. The resulting six CDB files per femur are then loaded in ANSYS Mechanical APDL, where static FE simulations are performed to obtain the maximum principal strain ( $\epsilon_1$ ) and minimum principal strain ( $\epsilon_3$ ) at the nodes corresponding to the experimental positions of the strain gauges.

## 2.3.7 Finite Element Analysis

In ANSYS Mechanical APDL, an identical analysis workflow was applied to all configurations of each femur. During the pre-processing, to replicate the experimental procedure and account for the configuration-dependent inclination, a local reference system was defined based on the rotation angles with respect to the frontal and sagittal axes.

Rotations in the frontal plane (LC2, LC4, LC6) use a negative  $\alpha$  for both right and left femora under the adopted convention. Concerning rotations in the sagittal plane, flexion (LC1) uses positive  $\beta$  for right femurs and negative  $\beta$  for left femora, whereas extension (LC3) follows the opposite sign.

The mesh was constrained in the local reference frame by fully fixing all nodes in the distal region, defined as  $z \le zth$ , where:

$$zth = z_{max,head} - 0.33 * BL - 100mm$$

 $z_{max,head}$  is the highest z coordinate at the head of the femur and BL is the biomechanical length obtained for each femur in the MATLAB protocol, as specified in [36]. The applied constraints concerned only the translational degrees of freedom (DOFs) ux, uy, and uz, as the element type SOLID187 does not present rotational DOFs; thus ux=0, uy=0, and uz=0 were set.



Figure 2.3-28. The constraints from  $zth = z_{max,head} - 0.33 * BL - 100mm$  up to the point with the lowest z-coordinate are applied on LC5 (neutral configuration) for femur #3154. The femur is rotated by  $0^{\circ}$  in the frontal plane and  $0^{\circ}$  in the sagittal plane. Constrains are defined within a local reference system that accounts for this rotation.

Within the local cartesian system, the node on the femoral head with the greatest z-coordinate was selected as the point of load application. Because five experimental trials were performed for each configuration, the load magnitude used in the simulations was set to the mean of the five measured forces.

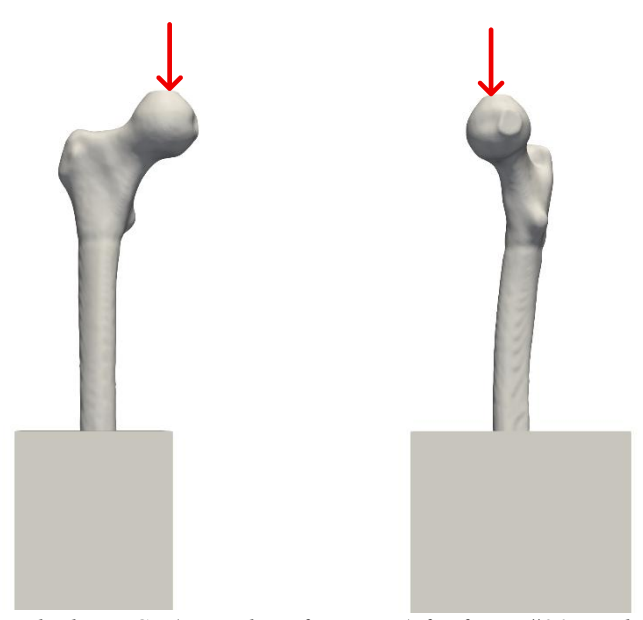


Figure 2.3-29. The force is applied on LC5 (neutral configuration) for femur #3154. The femur is rotated by 0° in the frontal plane and 0°in the sagittal plane. The load is applied along the global z-axis in order to replicate the experimental procedure. Both the XZ-plane (a) and YZ-plane (b) visualizations are shown.

The region of interest (ROI) to analyze the strain distribution has been therefore defined as the external corner nodes (thus excluding the midnodes of the external elements) of the unconstrained region.

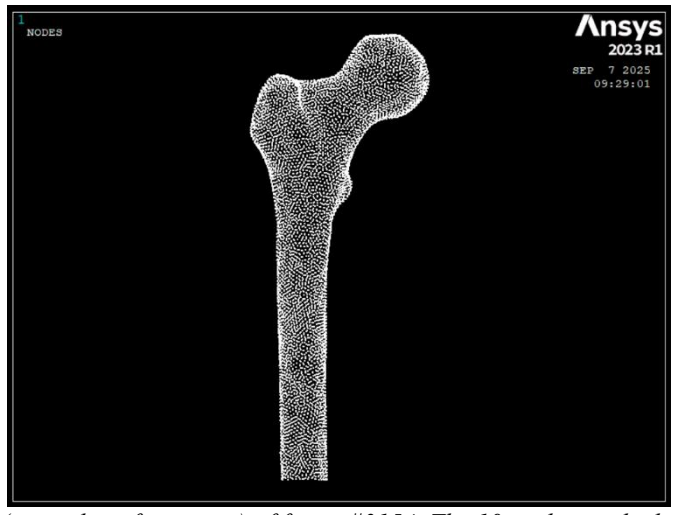


Figure 2.3-30. ROI for LC5 (neutral configuration) of femur #3154. The 10-node tetrahedral elements forming the mesh are second-order elements, meaning that additional nodes are located at the midpoints of each edge of the tetrahedron.

These mid-edge nodes are not considered when selecting the ROI.

In the following figure the constraints and the application of the force are shown for femur #3154 in all six loading configurations.

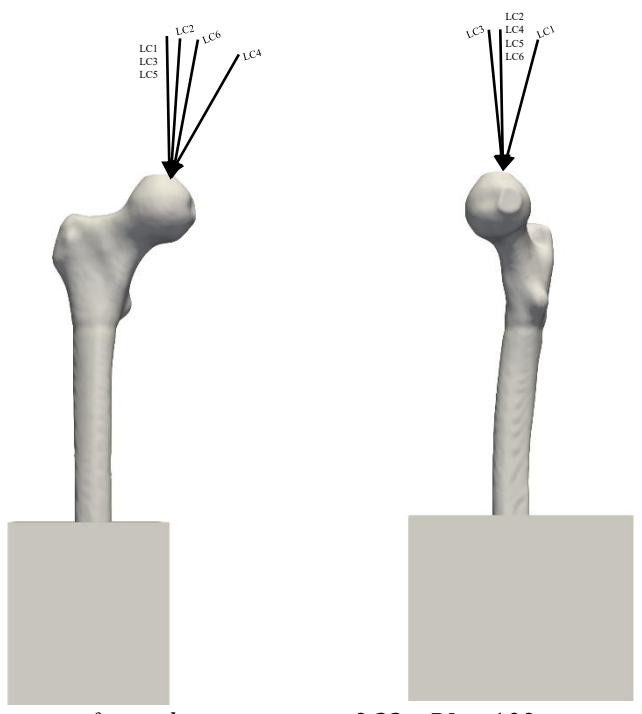


Figure 2.3-31. The constraints from  $zth = z_{max,head} - 0.33 * BL - 100mm$  up to the point with the lowest z-coordinate are applied femur #3154. Constrains are defined within a local reference system that accounts for this rotation. The six loading configurations are shown. Load application is carried out within the global reference system.

After preprocessing, the model is solved using a nonlinear static analysis with large displacements. The load is applied with automatic time stepping: 10 initial substeps, adaptively varied between a minimum of 5 and a maximum of 100 to aid convergence. Up to 500 equilibrium iterations per substep are allowed, with line search enabled to stabilize the convergence of the solution. Results are saved at the last substep.

In post-processing, the first and third principal strain fields ( $\varepsilon_1$  and  $\varepsilon_3$ ) are evaluated within the ROI. To extract values at the nodes corresponding to the experimental strain-gauge locations, the nodal solution is averaged over a 3 mm radius spherical neighborhood, restricted to nodes contained within the ROI. This local averaging ensures continuity of the strain field and mitigates mesh-dependent or highly localized effects [39]. In order to do so, a spherical reference system, with a 3mm radius, has been centered in each node corresponding to the strain gauges experimental position, and the strains of the ROI nodes falling in this tributary surface have been averaged. This post-processing approach was validated with a MATLAB routine that, given the ROI nodes coordinates and their first and third

principal strains ( $\varepsilon_1$  and  $\varepsilon_3$ ), constructs a proximity matrix and computes the mean strain over all nodes within the 3 mm cutoff.

## 2.3.8 Comparison between predicted and experimental values

To compare computational predictions with experimental measurements, model accuracy was quantified by the root-mean-square error (RMSE) and the maximum absolute (peak) error, with both metrics also reported as percentages of the maximum measured strain magnitude; in addition, the mean percentage error was computed over  $\varepsilon_1$  and  $\varepsilon_3$  for each strain gauge, pooled across the six loading configurations and the four femora under investigation.

The RMSE has been computed as:

$$RMSE = \sqrt[2]{\frac{1}{n} * \sum_{i}^{n} (y_i - x_i)^2}$$

Where  $y_i$  is the predicted value,  $x_i$  is the experimental value and n the number of observations.

The maximum peak error has been calculated as:

$$Maximum\ Peak\ Error = \max{(|y_i - x_i|)}$$

Where  $y_i$  is the predicted values and  $x_i$  is the experimental value.

Percentage RMSE and percentage maximum peak error were computed as percentages of the maximum measured strain magnitude, which is calculated as max ( $|x_i|$ ).

The mean percentage error for all strain gauges for each femur and across all femurs pooled together was first computed for each strain gauges as:

Percentage Error = 
$$100 * \frac{\left|\varepsilon_i^{model} - \varepsilon_i^{experiment}\right|}{\left|\varepsilon_i^{experiment}\right|}$$
 for  $i = 1,3$ 

Subsequently, the percentage error for each strain gauge was averaged across all six loading configurations for each femur and finally for all femurs pooled together.

#### 3 RESULTS

For clarity, the chapter is structured into three main sections. The first presents the analysis of the results for each individual femur. The second examines paired interspecimen variability by pooling femurs #2920-#2921 and #3154-#3155, as well as unpaired interspecimen variability by pooling femurs #2921-#3154 and #2920-#3155. Finally, the third section combines the results from all femurs across all loading configurations.

## 3.1 Results per femur

In this section, for each femur, a linear regression is performed to assess how well experimental strains are predicted by the model, and the RMSE and maximum peak errors are computed both in  $\mu\epsilon$  and as percentage of the maximum measured strain in absolute values. The mean percentage error is first computed as well for each strain gauge for both  $\epsilon_1$  and  $\epsilon_3$ , and it is then averaged over all strain gauges by pooling all loading configurations. For comparability across specimens, the analysis includes only those strain gauges that are common to all femora.

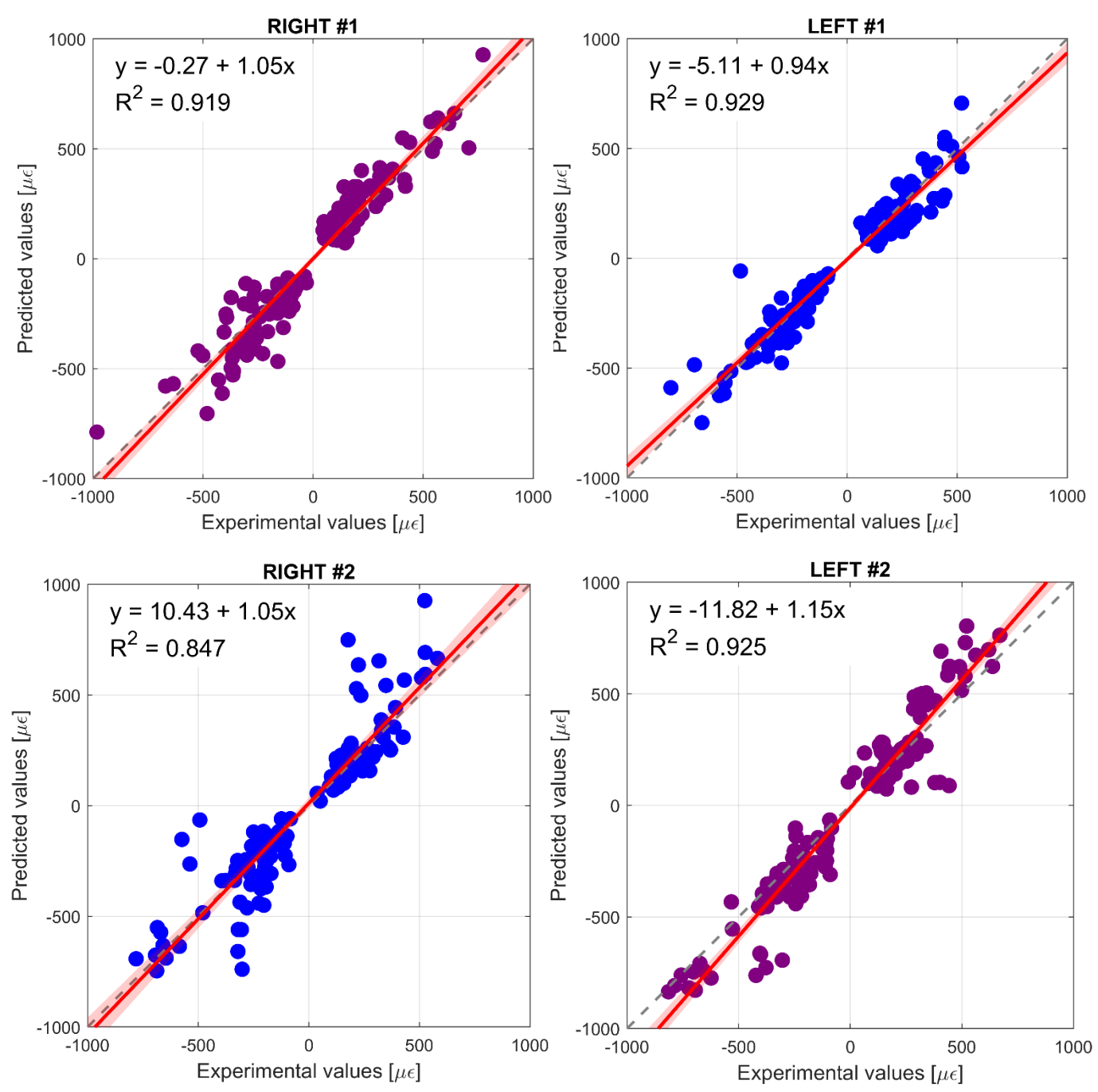


Figure 3.1-1. Scatter plots for the regression analyses, computed using only the strain gauges common to all femora. Data points for the femora with experimentally measured gauge locations—#3154 (Right 2) and #2921 (Left 1)—are shown in blue; data points for the remaining femora—#2920 (Right 1) and #3155 (Left 2)—are shown in purple.

Figure 3.1-1 illustrates the regression lines obtained for each femur when considering only the strain gauges common to all four specimens. For femurs #2920 (Right 1), 2921 (Left 1), and #3155 (Left 2), the models exhibit a close agreement with the experimental data, with coefficients of determination exceeding 0.91 and regression slopes and intercepts approaching 1 and 0, respectively. Femur #3154 (Right 2) yielded the lowest performance, with a coefficient of determination of 0.85; nevertheless, the regression slope and intercept remain close to one and zero, respectively.

# **FEMUR #2920 (RIGHT #1)**

$R^2$	0.92
Slope	1.05
Intercept (με)	-0.27
RMSE (με)	95.6
RMSE %	9.7
Max Error (με)	307.2
Max Error %	31.3
Mean Error %	44.7

Table 3.1-1. Validation Parameters for femur #2920 (Right 1)

# **FEMUR #2921 (LEFT #1)**

$R^2$	0.93
Slope	0.94
Intercept (με)	-5.11
RMSE (με)	82.3
RMSE %	10.3
Max Error (με)	426.9
Max Error %	53.3
Mean Error %	24.2

Table 3.1-2. Validation Parameters for femur #2921 (Left 1)

# **FEMUR #3154 (RIGHT #2)**

$R^2$	0.85
Slope	1.05
Intercept (με)	10.43
RMSE (με)	134.0
RMSE %	17.5
Max Error (με)	571.4
Max Error %	73.2
Mean Error %	37.3

Table 3.1-3. Validation Parameters for femur #3154 (Right 2)

#### **FEMUR #3155 (LEFT #2)**

$R^2$	0.93
Slope	1.15
Intercept (με)	-11.82
RMSE (με)	126.7
RMSE %	15.6
Max Error (με)	389.5
Max Error %	47.8
Mean Error %	49.4

Table 3.1-4. Validation Parameters for femur #3155 (Left 2)

With regard to prediction accuracy, femurs #2920 (Right 1) and #2921 (Left 1) achieved the best performance, with RMSE values below 10%, as reported in Tables 3.1-1 and 3.1-2. In contrast, the femurs from the second donor (#3154 – Right 1 and #3155 – Left 2) exhibited less satisfactory results, with RMSE values ranging between 16% and 18%, as shown in Tables 3.1-3 and 3.1-4.

The analysis of the mean percentage errors computed on the strain gauges highlights marked differences among the femurs. Femur #2921 (Left 1) exhibits the lowest mean error (24.2%), followed by femur #3154 (Right 2) with 37.3%. Higher values were observed for femur #2920 (Right 1) and femur #3155 (Left 2), which reached 44.7% and 49.3%, respectively. These results were expected, as the experimental strain gauge positions were available for femurs #2921 and #3154 only.

In spite of the difference among models in terms of accuracy, all of them consistently show higher tensile strains in the lateral part of the femur and in the lateral aspect of the neck, and higher compressive strains in the medial aspect of the femur, in agreement with findings reported in the literature [34]. Tensile strains reach peak values between 707 and 927 µɛ at the location of strain gauge LH, which has been identified as the most tensile-stressed site, consistently with previous studies [34]. Compressive strains attain peak values between 746 and 835 µɛ at the location of strain gauge M3.

## 3.2 Paired and un-paired interspecimen results

In this section we report results for the donor-matched pairs #2920–#2921 and #3154–#3155, as well as for the cross-donor pairs #2921–#3154 (the only two specimens with experimental coordinates of strain gauges available) and #2920–#3155. For each pair, model performance is quantified by the RMSE and the maximum absolute (peak) error, expressed both in microstrain (με) and normalized to the maximum absolute measured strain. The mean percentage error is computed per strain gauge (ε<sub>1</sub> and ε<sub>3</sub>) and then averaged across gauges and across the six loading configurations for the two femora. To ensure robust comparisons between paired and unpaired femora and between specimens with versus without experimental gauge locations, the analysis is restricted to the subset of strain gauges present on both femurs in each pair.

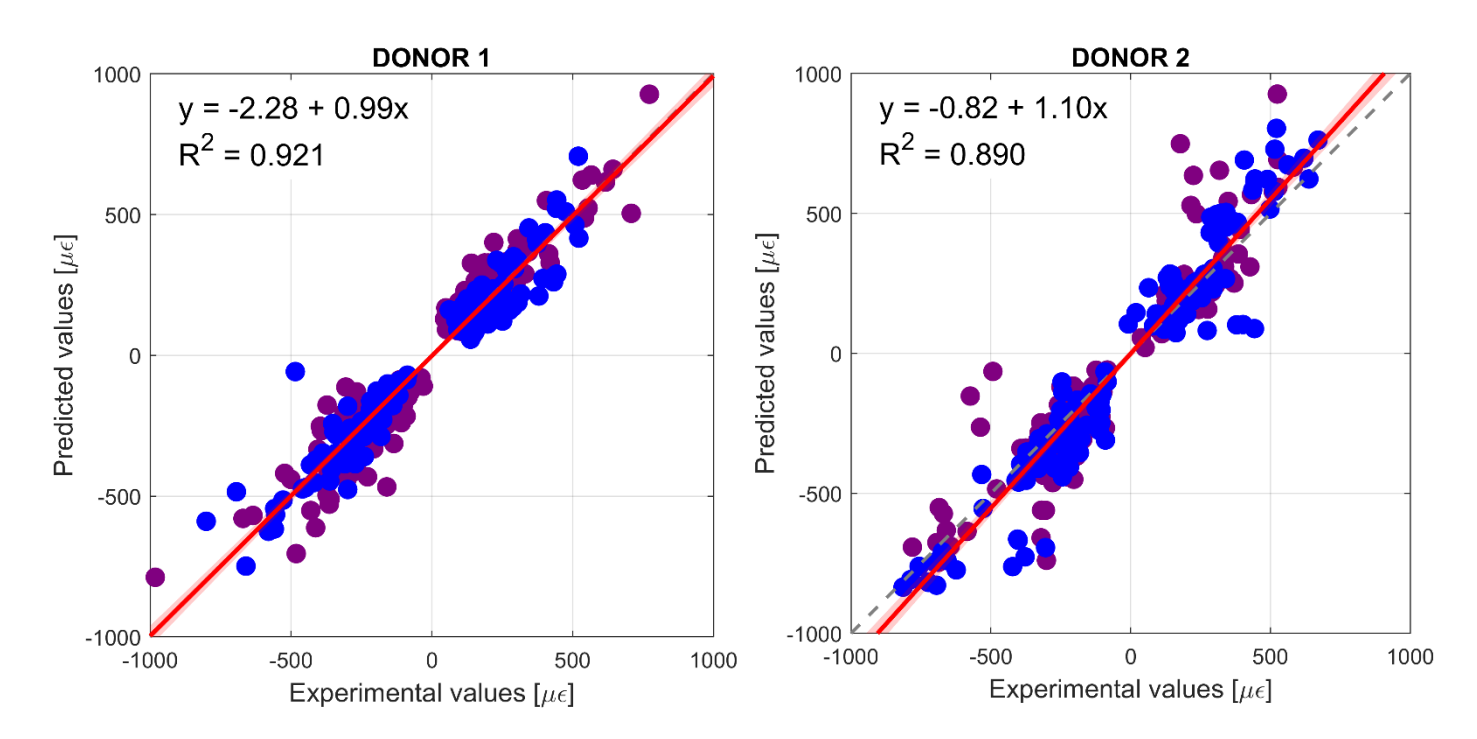


Figure 3.2-1. Linear regression of predicted strains vs experimental strains for paired femurs #2920-#2921 (Donor #1) and paired femurs #3154-#3155 (Donor #2). All strain measurements are plotted (\varepsilon\_1.and \varepsilon\_3) for all strain gauges present on both femurs in each pair. Left femurs (#2921- Left 1 and #3155-Left 2) are scattered in blue; data points for the right femurs ((#2920- Right 1 and #3154-Right 2) are shown in purple.

The regression lines presented in Figure 3.2-1 demonstrate a strong agreement for Donor 1, with an R<sup>2</sup> value of 0.92 and regression slope and intercept close to one and zero, respectively. Slightly poorer results are observed for Donor 2, whose coefficient of determination is just below 0.9. In this case, although the slope and intercept remain close to one and zero, the regression line indicates a minimal overestimation of the experimental strains.

#### **DONOR #1**

$R^2$	0.92
Slope	0.99
Intercept (με)	-2.28
RMSE (με)	89.2
RMSE %	9.1
Max Error (με)	426.9
Max Error %	43.5
Mean Error %	34.5

Table 3.2-1. Validation Parameters for Donor #1

#### **DONOR #2**

$R^2$	0.89
Slope	1.10
Intercept (με)	-0.82
RMSE (με)	134.4
RMSE %	16.3
Max Error (με)	571.4
Max Error %	70.2
Mean Error %	43.6

Table 3.2-2. Validation Parameters for Donor #2

For Donor 1, the RMSE is below 10% of the maximum measured strain, as reported in Table 3.2-1, which confirms the high predictive accuracy of the corresponding models. An RMSE below 10% is consistent with findings previously reported in the literature [26]. Although the mean percentage error is 34.5%, the low RMSE suggests that this value is mainly driven by localized discrepancies between experimental and predicted strains. In contrast, the predictive accuracy for Donor 2 is notably lower, as also reflected by the regression line in Figure 3.2-1. In this case, the RMSE reaches 16%, and the mean percentage error is higher as well (43.6%).

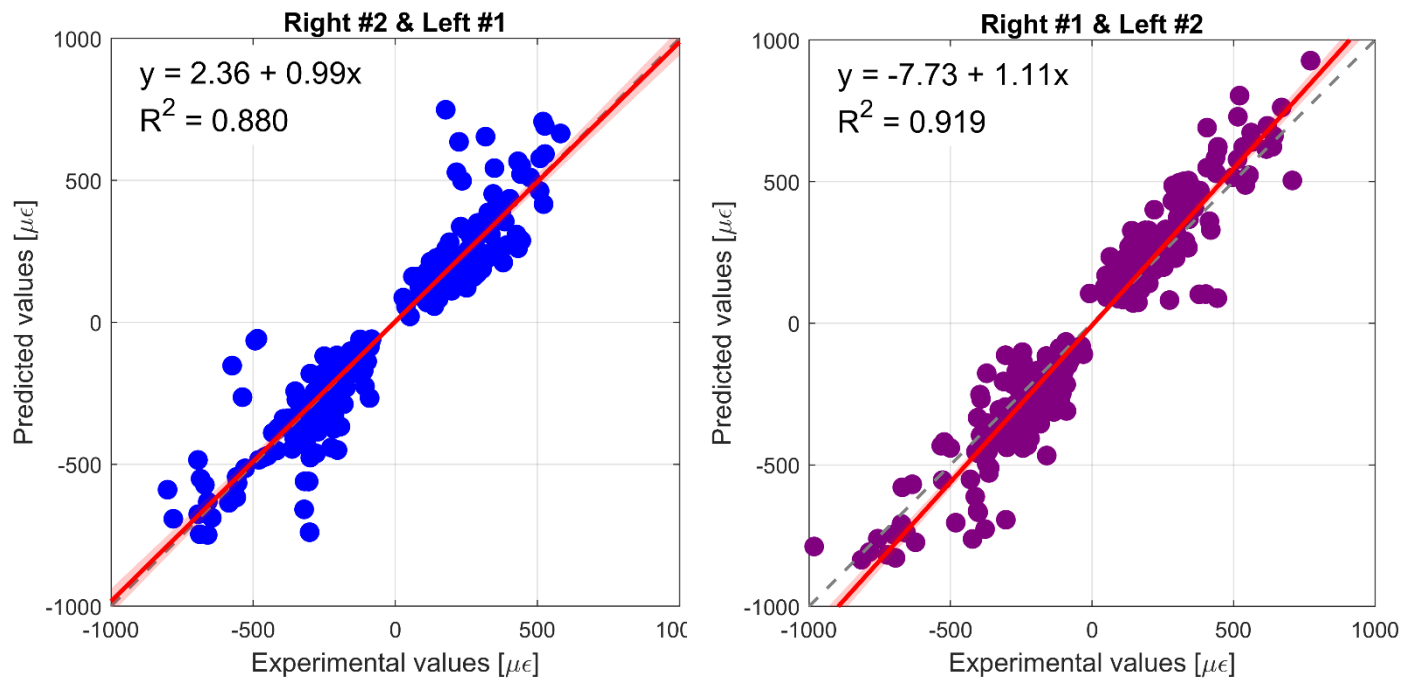


Figure 3.2-2. Regression lines obtained for two cross-pairs of femurs, highlighting the difference in predictive accuracy between specimens for which the experimental strain gauge positions were available (femurs #2921, Left 1, and #3154, Right 2; shown in blue) and those for which they were not (femurs #2920, Right 1, and #3155, Left 2; shown in purple).

Figure 3.3-2 illustrates the regression lines for the cross-paired femurs #2921–#3154 (Left 1–Right 2) and #2920–#3155 (Right 1–Left 2). The former pair exhibits a reasonably strong correlation between predicted and experimental strains, with a determination coefficient of 0.88, which is slightly lower compared to other cases. The regression slope (0.99) and intercept (2.36  $\mu\epsilon$ ) are very close to the ideal values of one and zero, respectively, indicating the absence of systematic bias. In contrast, the latter pair achieves a higher coefficient of determination (R<sup>2</sup> = 0.92), with slope and intercept also close to one and zero, although the slope suggests a systematic tendency to overestimate the experimental strains.

#### **FEMURS LEFT 1- RIGHT 2**

$R^2$	0.88
Slope	0.99
Intercept (με)	2.36
RMSE (με)	110.7
RMSE %	13.8
Max Error (με)	571.4
Max Error %	71.3
Mean Error %	30.8

Table 3.2-3. Validation Parameters for unpaired femurs #2921 (Left 1) and #3154 (Right 2), which were the only two femurs whose experimental strain gauges positions were available.

#### **FEMURS RIGHT 1- LEFT 2**

$R^2$	0.92
Slope	1.11
Intercept (με)	-7.73
RMSE (με)	112.2
RMSE %	11.4
Max Error (με)	389.5
Max Error %	39.7
Mean Error %	47.1

Table 3.2-4. Validation Parameters for unpaired femurs #2920 (Right 1) and #3155 (Left 2), whose experimental strain gauges positions were not available.

The two tables above (Tables 3.2-3 and 3.2-4) report the quantification of the prediction accuracy for femurs #2921-#3154 (Left 1- Right 2) and #2920-#3155 (Right 1 – Left 2) respectively. For former femurs #2921-#3154 (Left 1- Right 2) the RMSE is 110.7  $\mu\epsilon$  (13.8%), which can be considered acceptable though not optimal. The maximum error, however, reaches 571.4  $\mu\epsilon$  (71.3%), revealing localized discrepancies at specific strain gauges. For latter femurs #2920-#3155 (Right 1 – Left 2), the RMSE is comparable to the previous case (112.2  $\mu\epsilon$ , 11.4%), confirming an acceptable overall accuracy. The maximum error is lower (389.5  $\mu\epsilon$ , 39.7%) than that observed for #2921-#3154 (Left 1- Right 2) indicating that discrepancies at individual gauges are less extreme.

However, for femurs #2921-#3154 (Left 1- Right 2) the mean percentage error (30.8%) is comparatively lower to the other cross pair taken into consideration (for which a mean error of 47.1% is reported) and compared to the results for paired femurs. This can be explained by the fact that these two femurs were the only specimens for which the exact experimental strain gauge positions were available, thereby improving the accuracy of the numerical—experimental comparison. These findings highlight the crucial importance of accurate strain gauge localization in the validation of finite element predictions against experimental data.

## 3.3 Results by pooling all femurs

In this section, the results from all four femurs are pooled together. As in the single-femur and paired/unpaired analyses, the error is quantified using both RMSE and maximum peak error, reported in terms of  $\mu\epsilon$  and as a percentage of the highest recorded strain, as well as average mean error across all gauges and all six loading configurations.

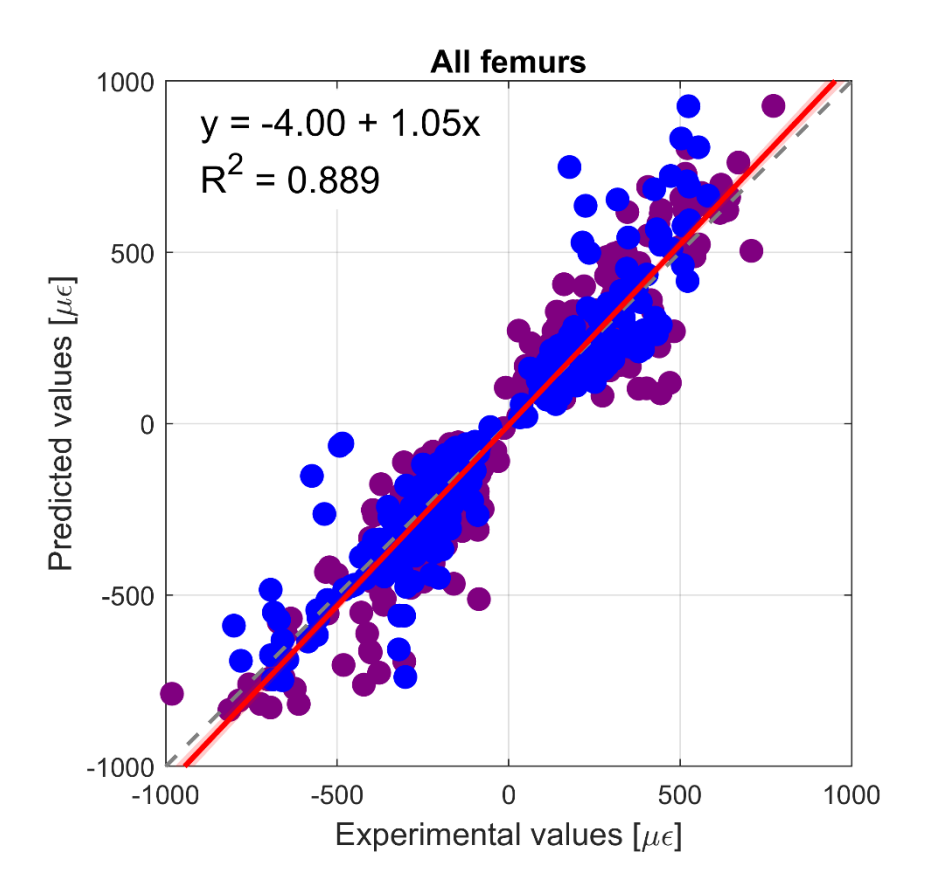


Figure 3.3-1. Linear regression of predicted strains vs experimental strains for all pooled femurs. All strain measurements are plotted ( $\varepsilon_1$  and  $\varepsilon_3$ ) for all strain gauges. Data points corresponding to femurs with experimentally verified strain gauge locations are shown in blue, while those from the other two femurs are represented in purple.

#### **ALL FEMURS**

$R^2$	0.89
Slope	1.05
Intercept (με)	-4.0
RMSE (με)	118.0
RMSE %	12.0
Max Error (με)	571.4
Max Error %	58.2
Mean Error %	42.7

Table 3.3-1. Validation Parameters for all pooled femurs

Figure 3.3-1 shows the regression line for predicted versus experimental strains across all femora under investigation, while the corresponding validation parameters are reported in Table 3.3-1 The correlation between predicted and experimental strains is good ( $R^2 = 0.89$ ), with the regression line exhibiting a slope close to one and an intercept close to zero. Nonetheless, the RMSE is 118.0  $\mu\epsilon$  (corresponding to 12% of the maximum measured value), indicating that the overall predictive performance of the model is only slightly worse than results reported in the literature [26], where an RMSE of 113  $\mu\epsilon$  (RMSE =9.78% of the highest measured strain) is observed.

## 4 DISCUSSION

The aim of this thesis was to construct CT-based FE models of four human cadaveric femurs, reproducing the in-vitro experimental tests previously conducted on the same specimens to compare the models' predictions with the experimental outcomes. The four femurs were experimentally instrumented with up to 16 triaxial strain gauges to measure the maximum and minimum principal strains and were subjected to six loading configurations in the stance condition. The same boundary conditions were applied to the FE models and the maximum and minimum principal strains were computed at the nodes of the mesh matching the positions of the experimental strain gauges. Such values were averaged over a sphere with a 3 mm radius in order to avoid local effect and ensure continuity of the results.

To evaluate model accuracy, regression analyses were performed for each femur individually, for paired and unpaired femurs, and for all femurs pooled together across the six loading configurations, considering both maximum and minimum principal strains. Errors were quantified in terms of RMSE and maximum peak error, reported both in microstrain and as a percentage of the maximum absolute experimental strain. In addition, mean percentage error was computed per strain gauge ( $\epsilon_1$  and  $\epsilon_3$ ) and then averaged across gauges and across the six loading configurations.

The results for individual indicate that the models predict experimental strains with good reliability, as the regression lines for each femur generally show coefficients of determination ( $R^2$ ) above 0.9, with slopes close to one and intercepts close to zero, once outlier strain gauges were excluded. The only exception is femur #3154 (Right 2), which demonstrates more limited predictive accuracy ( $R^2$  of 0.85); however, this discrepancy is attributable to strain gauge LH only which shows the highest percentage mean errors. Nonetheless, the models consistently predict peak tensile strains at strain gauge LH, in agreement with literature findings [34]. Furthermore, the strain distribution predicted by the models present in general higher tensile strains at the lateral aspect of the femur and higher compressive strains on the medial aspect, which is in agreement with findings reported in the literature [32].

Concerning the mean percentage errors, the lowest discrepancies were observed for femurs #2921 (Left 1) and #3154 (Right 2), which exhibited mean percentage errors of 24% and 37%, respectively, while the other two femurs showed values exceeding 40%. This difference becomes even more evident when comparing the cross-paired femurs: the first pair (#2921–#3154) presented an overall mean error of 31%, whereas the second pair (#2920- #3155) showed a substantially higher error of 47%. This discrepancy can be attributed to the fact that, for the first cross pair, experimental strain

gauges locations were available, thereby ensuring a more accurate correspondence between measured and predicted values.

Results for all femurs pooled together show a good agreement between predicted and experimental strains, with an  $R^2$  of 0.89 and a regression line slope and intercept not substantially different from one and zero, respectively. The RMSE corresponds to 12% of the highest measured strain, which is only slightly worse than the values reported in the literature [27], where an RMSE just below 10% of the highest measured strain has been observed. This discrepancy may be attributable to uncertainties inherent in the segmentation process or in the strain gauge measurements. Furthermore, the aforementioned study validated the finite element models on a sample size twice as large as that considered in the present work [26].

# **5 CONCLUSION**

In conclusion, the models developed in this thesis successfully replicate the experimental procedure and predict the maximum and minimum principal strains with satisfactory accuracy. They also reliably reproduce the overall strain distribution within the femur when subjected to stance loading conditions. Future developments may include a more refined segmentation process to improve the predictive accuracy of the models, as well as the analysis of a larger pool of femurs to strengthen the robustness of the results. Furthermore, the methodology could be extended to additional loading conditions, such as those replicating falls, which represent the most common scenarios leading to hip fractures in osteoporotic subjects [17].

## REFERENCES

- [1] U. N. Mughal, H. A. Khawaja, e M. Moatamedi, «Finite element analysis of human femur bone», *Int. J. Multiphysics*, vol. 9, fasc. 2, pp. 101–108, giu. 2015, doi: 10.1260/1750-9548.9.2.101.
- [2] S. M. A. Shah e S. N. Fatima, «GENERAL AND COMPARATIVE ANATOMY OF FEMUR».
- [3] Associate professor, Department of Anatomy, Narayan Medical College, Sasaram, Bihar, India. *et al.*, «Study of Dimensions of Head and Neck of Human Femur and its Clinical Significance», *Int. J. Anat. Res.*, vol. 10, fasc. 2, pp. 8359–8362, giu. 2022, doi: 10.16965/ijar.2022.140.
- [4] Office of the Surgeon General (US), *Bone Health and Osteoporosis: A Report of the Surgeon General*. in Reports of the Surgeon General. Rockville (MD): Office of the Surgeon General (US), 2004. Consultato: 19 maggio 2025. [Online]. Disponibile su: http://www.ncbi.nlm.nih.gov/books/NBK45513/
- [5] J. Dj. Black e B. J. Tadros, «Bone structure: from cortical to calcium», *Orthop. Trauma*, vol. 34, fasc. 3, pp. 113–119, giu. 2020, doi: 10.1016/j.mporth.2020.03.002.
- [6] P. T. Cowan, M. V. Launico, e P. Kahai, «Anatomy, Bones», in *StatPearls*, Treasure Island (FL): StatPearls Publishing, 2025. Consultato: 19 maggio 2025. [Online]. Disponibile su: http://www.ncbi.nlm.nih.gov/books/NBK537199/
- [7] N. H. Hart *et al.*, «Biological basis of bone strength: anatomy, physiology and measurement», *J. Musculoskelet. Neuronal Interact.*, vol. 20, fasc. 3, pp. 347–371, set. 2020.
- [8] R. Florencio-Silva, G. R. D. S. Sasso, E. Sasso-Cerri, M. J. Simões, e P. S. Cerri, «Biology of Bone Tissue: Structure, Function, and Factors That Influence Bone Cells», *BioMed Res. Int.*, vol. 2015, pp. 1–17, 2015, doi: 10.1155/2015/421746.
- [9] M. Fontcuberta-Rigo, M. Nakamura, e P. Puigbò, «Phylobone: a comprehensive database of bone extracellular matrix proteins in human and model organisms», *Bone Res.*, vol. 11, fasc. 1, p. 44, ago. 2023, doi: 10.1038/s41413-023-00281-w.
- [10] Vari, «Tessuto Osseo».
- [11] R. Oftadeh, M. Perez-Viloria, J. C. Villa-Camacho, A. Vaziri, e A. Nazarian, «Biomechanics and mechanobiology of trabecular bone: a review», *J. Biomech. Eng.*, vol. 137, fasc. 1, pp. 0108021–01080215, gen. 2015, doi: 10.1115/1.4029176.
- [12] F. Taddei, L. Cristofolini, S. Martelli, H. S. Gill, e M. Viceconti, «Subject-specific finite element models of long bones: An in vitro evaluation of the overall accuracy», *J. Biomech.*, vol. 39, fasc. 13, pp. 2457–2467, gen. 2006, doi: 10.1016/j.jbiomech.2005.07.018.
- [13] D. M. Cullinane e T. A. Einhorn, «Biomechanics of Bone», in *Principles of Bone Biology*, Elsevier, 2002, pp. 17–32. doi: 10.1016/B978-012098652-1.50104-9.
- [14] J. M. Kling, B. L. Clarke, e N. P. Sandhu, «Osteoporosis Prevention, Screening, and Treatment: A Review», *J. Womens Health*, vol. 23, fasc. 7, pp. 563–572, lug. 2014, doi: 10.1089/jwh.2013.4611.
- [15] J. H. Keyak *et al.*, «Male–female differences in the association between incident hip fracture and proximal femoral strength: A finite element analysis study», *Bone*, vol. 48, fasc. 6, pp. 1239–1245, giu. 2011, doi: 10.1016/j.bone.2011.03.682.
- [16] L. Cristofolini, E. Schileo, M. Juszczyk, F. Taddei, S. Martelli, e M. Viceconti, «Mechanical testing of bones: the positive synergy of finite–element models and *in vitro* experiments», *Philos. Trans. R. Soc. Math. Phys. Eng. Sci.*, vol. 368, fasc. 1920, pp. 2725–2763, giu. 2010, doi: 10.1098/rsta.2010.0046.
- [17] L. Zani, P. Erani, L. Grassi, F. Taddei, e L. Cristofolini, «Strain distribution in the proximal Human femur during in vitro simulated sideways fall», *J. Biomech.*, vol. 48, fasc. 10, pp. 2130–2143, lug. 2015, doi: 10.1016/j.jbiomech.2015.02.022.

- [18] L. Cristofolini, M. Juszczyk, S. Martelli, F. Taddei, e M. Viceconti, «In vitro replication of spontaneous fractures of the proximal human femur», *J. Biomech.*, vol. 40, fasc. 13, pp. 2837–2845, 2007, doi: 10.1016/j.jbiomech.2007.03.015.
- [19] M. Qasim *et al.*, «Patient-specific finite element estimated femur strength as a predictor of the risk of hip fracture: the effect of methodological determinants», *Osteoporos. Int.*, vol. 27, fasc. 9, pp. 2815–2822, set. 2016, doi: 10.1007/s00198-016-3597-4.
- [20] T. M. Link, «Osteoporosis imaging: state of the art and advanced imaging», *Radiology*, vol. 263, fasc. 1, pp. 3–17, apr. 2012, doi: 10.1148/radiol.2633201203.
- [21] P. R. Patel e O. De Jesus, «CT Scan», in *StatPearls*, Treasure Island (FL): StatPearls Publishing, 2025. Consultato: 17 agosto 2025. [Online]. Disponibile su: http://www.ncbi.nlm.nih.gov/books/NBK567796/
- [22] H. K. Genant, K. Engelke, e S. Prevrhal, «Advanced CT bone imaging in osteoporosis», *Rheumatol. Oxf. Engl.*, vol. 47 Suppl 4, fasc. Suppl 4, pp. iv9-16, lug. 2008, doi: 10.1093/rheumatology/ken180.
- [23] F. Taddei, S. Martelli, B. Reggiani, L. Cristofolini, e M. Viceconti, «Finite-Element Modeling of Bones From CT Data: Sensitivity to Geometry and Material Uncertainties», *IEEE Trans. Biomed. Eng.*, vol. 53, fasc. 11, pp. 2194–2200, nov. 2006, doi: 10.1109/TBME.2006.879473.
- [24] T. Fadiji, C. J. Coetzee, T. M. Berry, A. Ambaw, e U. L. Opara, «The efficacy of finite element analysis (FEA) as a design tool for food packaging: A review», *Biosyst. Eng.*, vol. 174, pp. 20–40, ott. 2018, doi: 10.1016/j.biosystemseng.2018.06.015.
- [25] E. Schileo, F. Taddei, L. Cristofolini, e M. Viceconti, «Subject-specific finite element models implementing a maximum principal strain criterion are able to estimate failure risk and fracture location on human femurs tested in vitro», *J. Biomech.*, vol. 41, fasc. 2, pp. 356–367, 2008, doi: 10.1016/j.jbiomech.2007.09.009.
- [26] E. Schileo, F. Taddei, A. Malandrino, L. Cristofolini, e M. Viceconti, «Subject-specific finite element models can accurately predict strain levels in long bones», *J. Biomech.*, vol. 40, fasc. 13, pp. 2982–2989, 2007, doi: 10.1016/j.jbiomech.2007.02.010.
- [27] F. Taddei, E. Schileo, B. Helgason, L. Cristofolini, e M. Viceconti, «The material mapping strategy influences the accuracy of CT-based finite element models of bones: an evaluation against experimental measurements», *Med. Eng. Phys.*, vol. 29, fasc. 9, pp. 973–979, nov. 2007, doi: 10.1016/j.medengphy.2006.10.014.
- [28] E. Schileo *et al.*, «An accurate estimation of bone density improves the accuracy of subject-specific finite element models», *J. Biomech.*, vol. 41, fasc. 11, pp. 2483–2491, ago. 2008, doi: 10.1016/j.jbiomech.2008.05.017.
- [29] A. Aldieri, C. Curreli, J. A. Szyszko, A. A. La Mattina, e M. Viceconti, «Credibility assessment of computational models according to ASME V&V40: Application to the Bologna Biomechanical Computed Tomography solution», *Comput. Methods Programs Biomed.*, vol. 240, p. 107727, ott. 2023, doi: 10.1016/j.cmpb.2023.107727.
- [30] L. Cristofolini, F. Taddei, M. Baleani, F. Baruffaldi, S. Stea, e M. Viceconti, «Multiscale investigation of the functional properties of the human femur», *Philos. Trans. R. Soc. Math. Phys. Eng. Sci.*, vol. 366, fasc. 1879, pp. 3319–3341, set. 2008, doi: 10.1098/rsta.2008.0077.
- [31] L. Cristofolini *et al.*, «DIFFERENCES BETWEEN CONTRALATERAL BONES OF THE HUMAN LOWER LIMBS: A MULTISCALE INVESTIGATION», *J. Mech. Med. Biol.*, vol. 14, fasc. 03, p. 1450032, giu. 2014, doi: 10.1142/S0219519414500328.
- [32] C. B. Ruff e W. C. Hayes, «Cross-sectional geometry of Pecos Pueblo femora and tibiae—A biomechanical investigation: I. Method and general patterns of variation», *Am. J. Phys. Anthropol.*, vol. 60, fasc. 3, pp. 359–381, mar. 1983, doi: 10.1002/ajpa.1330600308.
- [33] Cristofolini, «IMPLANT STABILITY OF HIP STEMS».

- [34] L. Cristofolini, M. Juszczyk, F. Taddei, e M. Viceconti, «Strain distribution in the proximal human femoral metaphysis», *Proc. Inst. Mech. Eng. [H]*, vol. 223, fasc. 3, pp. 273–288, mar. 2009, doi: 10.1243/09544119JEIM497.
- [35] L. Cristofolini, G. Conti, M. Juszczyk, S. Cremonini, S. V. Sint Jan, e M. Viceconti, «Structural behaviour and strain distribution of the long bones of the human lower limbs», *J. Biomech.*, vol. 43, fasc. 5, pp. 826–835, mar. 2010, doi: 10.1016/j.jbiomech.2009.11.022.
- [36] G. Cammertoni, «Misura in vitro delle sollecitazioni in femori intatti e in condizioni di carico fisiologiche», ALMA MATER STUDIORUM UNIVERSITÀ DI BOLOGNA, 2010.
- [37] L. Cristofolini, B. P. McNamara, A. Freddi, e M. Viceconti, «*In vitro* measured strains in the loaded femur: Quantification of experimental error», *J. Strain Anal. Eng. Des.*, vol. 32, fasc. 3, pp. 193–200, apr. 1997, doi: 10.1243/0309324971513337.
- [38] T. D. DenOtter e J. Schubert, «Hounsfield Unit», in *StatPearls*, Treasure Island (FL): StatPearls Publishing, 2025. Consultato: 31 luglio 2025. [Online]. Disponibile su: http://www.ncbi.nlm.nih.gov/books/NBK547721/
- [39] E. Schileo, L. Balistreri, L. Grassi, L. Cristofolini, e F. Taddei, «To what extent can linear finite element models of human femora predict failure under stance and fall loading configurations?», *J. Biomech.*, vol. 47, fasc. 14, pp. 3531–3538, nov. 2014, doi: 10.1016/j.jbiomech.2014.08.024.